

# **Comprehensive Probabilistic Seismic Hazard Assessment for the East Anatolian Fault Zone: A Multi-Segment Rupture Framework Validated by the 2023 Kahramanmaraş Earthquake Sequence**

**Abstract:** The East Anatolian Fault Zone, a continental transform boundary within the Arabia-Eurasia collision zone, presents fundamental challenges for seismic hazard assessment due to complex structural segmentation and demonstrated cascading multi-segment rupture mechanisms. This investigation develops a comprehensive probabilistic seismic hazard assessment (PSHA) framework for the East Anatolian Fault Zone (EAFZ), incorporating novel multi-segment rupture scenarios that address demonstrated cascading failure potential observed during the 6 February 2023 Mw 7.8 Kahramanmaraş earthquake sequence. The PSHA implementation through OpenQuake Engine employs a systematic 162-branch logic tree quantifying epistemic uncertainties across three source-model configurations: Individual Segments Model (ISM), Limited Multi-Segment Model (LMSM), and Extensive Multi-Segment Model (EMSM), combined with six regionally calibrated ground-motion prediction equations. Regional PSHA reveals severe seismic exposure with peak ground accelerations approaching 2.0g for 2475-year return periods along well-defined high-hazard corridors. Critical urban centers exhibit substantial exposure: 475-year rock-site PGA values of 0.567g (Elazığ) and 0.557g (Hatay/Antakya) exceed conventional design spectra. Spectral acceleration analysis reveals pronounced period-dependent characteristics with short-period SA(0.3s) exceeding 2.2g and significant intermediate-period basin amplification reaching 0.98g. Disaggregation analysis identifies systematic site-specific controlling earthquake scenarios, with near-source locations dominated by proximal large-magnitude events while off-fault sites depend on distant high-magnitude scenarios. Physics-based simulation (PBS) provides independent validation of the computational modeling framework against comprehensive strong-motion datasets from the 2023 earthquake sequence using high-resolution SPECFEM3D. The validation demonstrates exceptional accuracy at intermediate distances (20–80 km) with synthetic–observed amplitude deviations within 10–20%, while identifying systematic near-fault underestimation reflecting kinematic source parameterization limitations. This validation establishes confidence in the regional velocity structure and fault parameterization employed within the probabilistic hazard

assessment. This research establishes quantitative methodological frameworks for multi-segment rupture assessment with direct implications for regional seismic design criteria .

**Keywords:** Seismic hazard assessment, Physics-based simulation, Probabilistic Seismic Hazard Assessment, East Anatolian Fault Zone , Multi-segment rupture

## Introduction

Seismic hazard assessment for complex fault systems represents one of the most challenging problems in contemporary earthquake science, requiring sophisticated methodologies capable of capturing the intricate interactions between fault geometry, rupture dynamics, and ground motion generation across multiple spatial and temporal scales. Continental transform systems, characterized by segmented architectures and complex rupture behaviors, pose particular difficulties for conventional assessment approaches that traditionally rely on simplified source representations and independent segment assumption (Field et al., 2014; Stirling et al., 2012). The fundamental challenge lies in developing reliable methodologies that can simultaneously address detailed wave propagation physics while systematically quantifying the inherent uncertainties associated with earthquake source processes and their resulting ground motion characteristics.

Physics-based simulation methodologies employ advanced numerical techniques to model seismic wave generation and propagation through heterogeneous crustal media, providing unprecedented resolution of ground motion characteristics in geometrically complex fault systems. These approaches utilize sophisticated computational frameworks including finite difference, finite element, and spectral element methods to solve the elastic wave equation across three-dimensional velocity structures, explicitly accounting for realistic fault geometries, rupture kinematics, and basin amplification effects (Graves & Pitarka, 2016; Rodgers et al., 2019; Taborda & Bielak, 2014). Physics-based simulations excel in capturing near-fault directivity phenomena, complex wave interference patterns, and frequency-dependent site response that empirical ground motion prediction equations struggle to reproduce (Olsen et al., 2006; Withers et al., 2019). However, these methodologies face fundamental constraints from substantial computational demands limiting frequency resolution and domain extent, critical uncertainties in kinematic source parameterization including slip distribution and rupture velocity specification, and incomplete characterization of three-dimensional crustal velocity structures particularly at shallow depths where impedance contrasts dominate site response (Graves et al., 2011; Taborda et al., 2016).

Probabilistic seismic hazard analysis provides systematic frameworks for quantifying earthquake ground motion exceedance probabilities through rigorous integration over magnitude-distance-source parameter spaces, incorporating epistemic uncertainty via logic tree methodologies that weight alternative source characterizations and ground motion models (Baker, 2013; Cornell, 1968; McGuire, 2004). PSHA implementations standardize seismic design ground motion specification for building codes and critical infrastructure through uniform hazard spectra and conditional mean spectra derived from comprehensive regional seismicity catalogs and validated ground motion prediction equations (Bradley, 2013; Stewart et al., 2015). Despite these strengths, conventional PSHA frameworks traditionally impose independence assumptions on fault segment rupture probabilities, potentially underestimating hazard contributions from cascading multi-segment earthquakes demonstrated by recent continental transform events including the 2016 Kaikōura sequence and 2023 Kahramanmaraş doublet (Biasi & Wesnousky, 2017; Field et al., 2014). Contemporary research initiatives increasingly employ complementary physics-based and probabilistic approaches to address complex rupture scenarios while maintaining rigorous uncertainty quantification. While physics-based simulations provide detailed ground motion characterization for specific events, probabilistic frameworks enable systematic hazard assessment across extended return periods, with comprehensive validation against major earthquake observations essential for establishing computational reliability (Bayless & Abrahamson, 2019; Graves & Pitarka, 2015).

Critical gaps persist in current seismic hazard assessment frameworks that fundamentally limit their reliability and applicability to segmented fault systems worldwide. First, conventional PSHA implementations inadequately address multi-segment rupture potential, despite growing evidence from recent major earthquakes that complex strike-slip systems can exhibit cascading failure mechanisms across traditional segmentation boundaries, fundamentally challenging the independence assumptions underlying standard probabilistic formulations (Biasi & Wesnousky, 2016). Second, physics-based simulation validation remains severely constrained by the scarcity of well-recorded large-magnitude events with comprehensive strong-motion datasets, particularly for continental transform systems where near-fault observations are historically rare and validation opportunities are limited (Graves & Pitarka, 2016). Third, epistemic uncertainty quantification in complex fault systems lacks systematic treatment of source model variations and their systematic propagation through hazard calculations, resulting in potentially significant underestimation of uncertainty bounds critical for risk-informed decision making (Marzocchi et al., 2015). These fundamental limitations compromise the reliability of seismic hazard estimates essential for critical

infrastructure design, building code development, and emergency preparedness applications across seismically active regions globally.

The catastrophic February 6, 2023, Kahramanmaraş earthquake sequence comprising an Mw 7.8 mainshock followed by an Mw 7.6 event nine hours later represents an unprecedented opportunity to address these fundamental methodological limitations through comprehensive validation and methodological advancement. This devastating sequence resulted in approximately 59,259 fatalities across Turkey and Syria with estimated economic losses exceeding \$103 billion, making it one of the deadliest and most costly natural disasters in the region's recorded history (AFAD, 2023; Jia et al., 2023; UNDP, 2023). The event fundamentally challenged conventional seismic hazard paradigms by demonstrating complex multi-segment rupture behavior spanning approximately 370 km across multiple fault segments, providing exceptional validation datasets for physics-based simulation, and necessitating fundamental revision of probabilistic source models to adequately capture demonstrated cascading failure potential (Barbot et al., 2023; Melgar et al., 2023). The comprehensive strong-motion recordings obtained during this sequence offer exceptional opportunities for systematic validation of computational approaches while advancing understanding of complex fault system behavior and ground motion generation processes.

This investigation addresses the identified research gaps through four specific objectives designed to advance seismic hazard assessment methodologies for complex fault systems: (1) validate the regional computational modeling framework through high-resolution physics-based simulation using SPECFEM3D (Komatitsch & Tromp, 2002; Peter et al., 2011) with comprehensive comparison against strong-motion observations from the 2023 earthquake to establish reliability benchmarks for the velocity structure, fault geometry, and computational approaches employed in regional hazard assessment. The SPECFEM3D Cartesian software package implements high-resolution seismic wave propagation modeling through the spectral element method a numerical technique combining the geometric flexibility of finite element approaches with the exponential convergence properties of spectral methods for accurate wavefield simulation in complex three-dimensional earth models. The investigation further seeks to (2) implement novel probabilistic seismic hazard assessment frameworks incorporating multi-segment rupture scenarios through systematic source model configurations that address demonstrated cascading failure potential; (3) quantify epistemic uncertainties through extensive logic tree analysis encompassing multiple source model variations and regionally calibrated ground motion prediction equations to provide comprehensive uncertainty characterization; and (4) establish comprehensive seismic hazard characterization

across multiple return periods and spectral parameters with detailed disaggregation analysis to identify controlling earthquake scenarios for engineering applications.

This paper is organized as follows: Section 2 presents the comprehensive geological and tectonic framework essential for understanding fault system complexity, Section 3 describes the probabilistic assessment and physics-based simulation validation methodologies, Section 4 provides comprehensive probabilistic seismic hazard assessment outcomes, Section 5 presents physics-based simulation validation results, Section 6 discusses methodology performance and implications for seismic hazard assessment practice, and Section 7 synthesizes key findings and their significance for advancing earthquake risk reduction in complex tectonic environments worldwide.

## **Geological And Tectonic Framework**

The methodological challenges identified for complex fault systems are exemplified by the East Anatolian Fault Zone (EAFZ), which represents one of the most seismically active continental transform systems globally and provides an ideal natural laboratory for advancing seismic hazard assessment methodologies. Understanding the comprehensive geological and tectonic framework of this system is essential for implementing sophisticated numerical modeling approaches that can adequately capture the complex interactions between fault architecture, crustal heterogeneities, and earthquake rupture processes. Figure 1 illustrates the regional tectonic framework of the East Anatolian Fault Zone within the broader Eastern Mediterranean neotectonic system. The EAFZ accommodates the westward extrusion of the Anatolian microplate through predominantly left-lateral strike-slip motion at geodetically determined rates of 9-10 mm/yr, extending approximately 580 km from the Karlıova Triple Junction to the Maraş Triple Junction (McClusky et al., 2000; Reilinger et al., 2006). This major tectonic structure constitutes a critical component of the Eastern Mediterranean's neotectonic framework, operating within the complex Arabia-Eurasia collision zone where convergence rates of 15-20 mm/yr drive systematic strain partitioning across multiple interconnected fault systems (Çetin et al., 2003; Westaway, 2003).

The EAFZ operates within a complex distributed deformation field characterized by systematic strain partitioning across multiple interconnected fault systems with distinct kinematic signatures (Faccenna et al., 2006; Westaway, 2004). GPS-derived velocity fields reveal that approximately 70% of the total plate motion is accommodated by the primary EAFZ strand, while the remaining 30% is distributed across secondary structures, most prominently

the Sürgü-Çardak fault system that parallels the main trace (Figure 2) (Aktuğ et al., 2016; Cavalié & Jónsson, 2014). This partitioning creates a fault zone architecture exhibiting systematic width variations from 5-10 km in northeastern segments to over 30 km in the southwestern region, reflecting progressive structural complexity toward the Eastern Mediterranean triple junction where multiple tectonic systems converge (Duman & Emre, 2013). Crustal architecture beneath the EAFZ demonstrates pronounced three-dimensional heterogeneities that fundamentally control seismic wave propagation characteristics during earthquake ruptures. Receiver function analysis integrated with local earthquake tomography reveals systematic Moho depth variations from 35-38 km beneath the Arabian foreland to 40-45 km beneath the elevated Anatolian Plateau, with notable localized thinning to 32 km beneath extensional pull-apart basins (Mutlu & Karabulut, 2011; Özcar et al., 2010; Tezel et al., 2013).

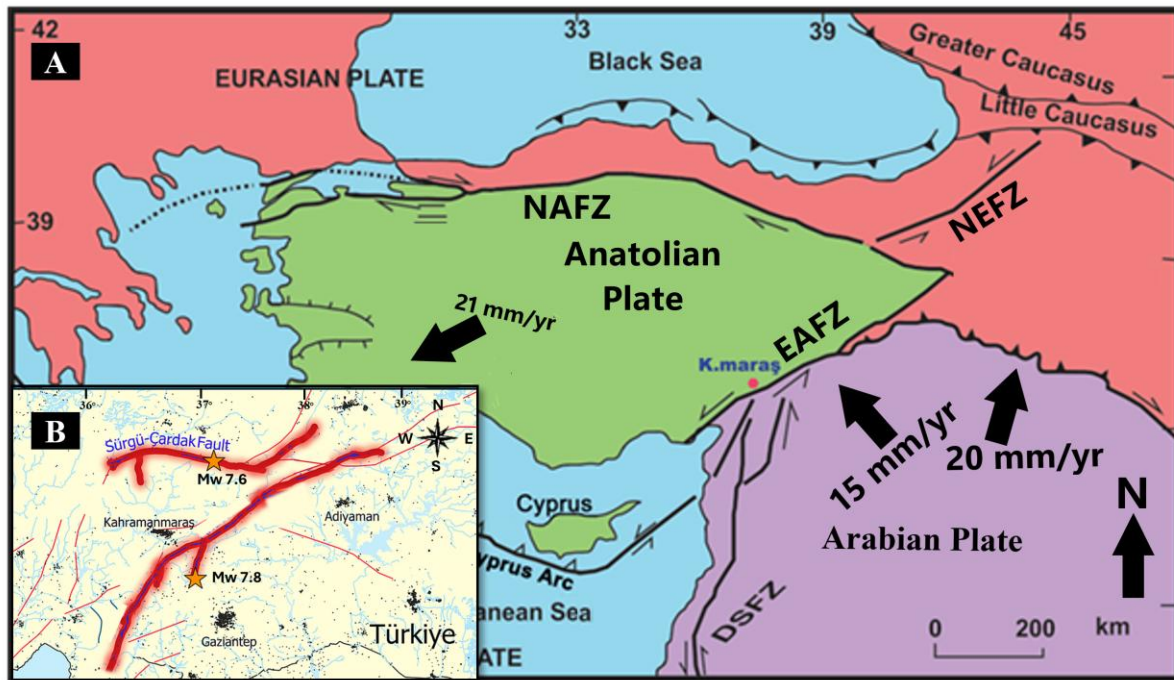


Figure 1. Regional tectonic framework of the East Anatolian Fault Zone. (A) Major plate boundaries and fault systems showing westward motion of the Anatolian Plate with convergence rates indicated by arrows. (B) February 6, 2023, Kahramanmaraş earthquake sequence showing Mw 7.8 and Mw 7.6 events with surface rupture zones

Upper crustal velocity structures exhibit dramatic lateral heterogeneities, with P-wave velocities ranging from 5.8-6.2 km/s in crystalline basement rocks to 2.5-4.5 km/s in thick sedimentary basin fills, creating impedance contrasts exceeding 50% that generate significant seismic wave amplification during earthquake events (Al-Lazki et al., 2003; Sandvol et al., 2003). These velocity variations, combined with complex fault zone damage structures,

establish heterogeneous waveguides that channel seismic energy and modify ground motion characteristics at regional scales (Ben-Zion & Sammis, 2003). Detailed structural analysis has delineated the EAFZ into thirteen distinct segments, each characterized by specific geometric parameters and seismogenic potential that govern earthquake generation characteristics (Figure 2) (Emre et al., 2018; Herece, 2008). Segment lengths vary substantially from 48 to 110 km, with seismogenic depths typically extending to 15-18 km based on microseismicity distributions (Kahraman et al., 2015). Geodetic observations reveal systematic along-strike slip rate variations from 8.5-9.5 mm/yr in northeastern segments to 4.0-6.0 mm/yr in southwestern segments, reflecting proximity to the Arabia-Anatolia Euler pole and strain partitioning with adjacent fault systems (Mahmoud et al., 2013; Reilinger et al., 2006). Segment boundaries defined by restraining bends, releasing stepovers, and structural junctions function as rupture barriers or nucleation zones that control earthquake magnitude distributions (Stein, 1999; Wesnousky, 2006).

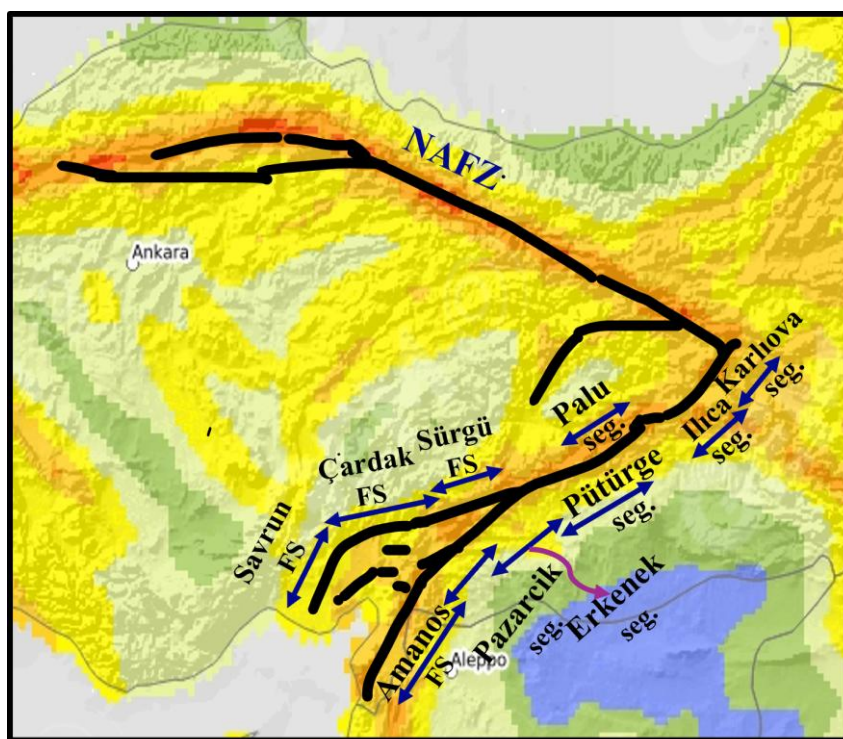


Figure 2. Topographic map of central eastern Türkiye illustrating the East Anatolian Fault Zone (EAFZ) and its principal structural segments including the Karlıova, İlica, Pazarcık–Nurdağı, Erkenek–Palu, and Çardak–Amanos segments (Duman & Emre, 2013) superimposed on shaded-relief terrain (Global Earthquake Model Foundation, 2025a)

The 2023 earthquake sequence involved sequential activation of the Nurdağı-Pazarcık and Erkenek segments during the Mw 7.8 mainshock, followed by rupture of the Çardak and Amanos segments during the subsequent Mw 7.6 event, demonstrating that traditional segment

boundaries can be transcended under critical stress conditions. Quantitative stress modeling indicates that the preceding 2020 Mw 6.7 Elazığ earthquake contributed measurable Coulomb stress increases on the Pazarcık segment prior to failure, exemplifying the stress transfer mechanisms that govern temporal earthquake clustering along the EAFZ (Pousse-Beltran et al., 2020).

## Methodology

This investigation employs a complementary dual-pathway framework to comprehensively evaluate seismic hazard across the East Anatolian Fault Zone, utilizing two methodologically distinct but synergistic approaches that maintain independent operational domains while providing mutual validation (Figure 3). The framework architecture comprises two parallel assessment pathways connected through a systematic validation protocol that establishes confidence in the computational infrastructure underlying both methodologies.

Probabilistic seismic hazard assessment (PSHA) constitutes the primary analytical framework, addressing the central innovation of this work through systematic quantification of multi-segment rupture potential via novel source model configurations (ISM, LMSM, EMSM). This regional-scale assessment explicitly treats the cascading failure mechanisms demonstrated by the 2023 earthquake sequence, fundamentally advancing beyond conventional segmentation paradigms that assume independent fault behavior. The PSHA implementation through OpenQuake Engine encompasses the complete spectrum of potential future rupture scenarios across extended return periods (50-2475 years) through systematic treatment of epistemic uncertainties via comprehensive logic tree methodology (162 branches), incorporating six regionally calibrated ground motion prediction equations (GMPEs) informed by regional seismo-tectonic characteristics. This probabilistic framework provides spatially distributed hazard characterization across the entire EAFZ region, enabling site-specific design ground motion specification for diverse urban centers and infrastructure applications.

Physics-based simulation (PBS) provides independent validation of the computational modeling framework through high-resolution wave propagation simulation of the 2023 Kahramanmaraş earthquake using SPECFEM3D. This near-field validation approach demonstrates that the regional seismo-tectonic framework including the 13-layer velocity structure, fault geometry parameterization, and crustal property specifications can accurately reproduce observed strong-motion characteristics with quantified reliability bounds. The PBS validation framework (Figure 3) establishes confidence in the fundamental computational

infrastructure shared between both methodologies, including crustal velocity architecture, attenuation parameters, and fault system geometry. By systematically comparing synthetic ground motions against comprehensive strong-motion datasets from the 2023 event, PBS quantifies modeling accuracy across varying distance ranges and geological conditions, thereby validating the regional framework subsequently employed within PSHA ground motion prediction.

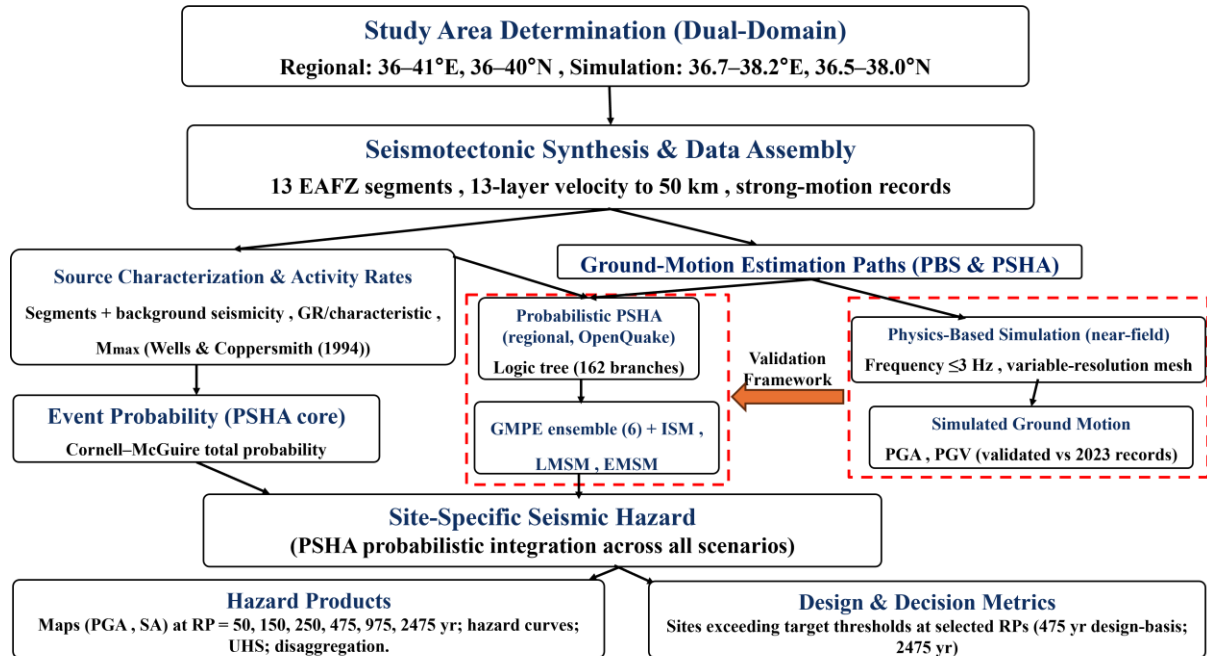


Figure 3. Complementary dual-pathway framework for seismic hazard assessment: Probabilistic hazard characterization (PSHA) and physics-based validation (PBS).

The complementary relationship between these methodologies (Figure 3) operates through distinct but mutually reinforcing pathways. PSHA quantifies probabilistic hazard across extended temporal and spatial scales encompassing all potential future earthquake scenarios, while PBS validates the reliability of computational modeling approaches for the specific EAFZ tectonic environment through comparison against actual earthquake observations. Critically, PBS does not generate probabilistic hazard estimates nor replace PSHA ground motion prediction; rather, it establishes the credibility of the modeling framework that informs regional hazard characterization. This dual-pathway architecture advances regional seismic hazard assessment by combining comprehensive probabilistic frameworks for multi-segment rupture quantification with physics-based validation benchmarking, addressing both the systematic quantification of uncertainties essential for engineering applications and the establishment of computational model reliability through empirical validation.

## 1. Probabilistic Seismic Hazard Assessment Framework

Probabilistic seismic hazard assessment (PSHA) provides a systematic framework for evaluating earthquake hazards by integrating four fundamental components: seismic source characterization, earthquake recurrence models, ground motion prediction equations, and probability calculations. This investigation implements comprehensive PSHA through the Cornell-McGuire total probability formulation with systematic logic tree analysis encompassing the complete EAFZ system, addressing regional-scale hazard assessment with rigorous epistemic uncertainty quantification. The EAFZ implementation incorporates advanced methodological developments in probabilistic hazard analysis, particularly robust treatment of epistemic uncertainties via logic trees and regionally calibrated ground motion prediction equations informed by the regional seismo-tectonic framework. This probabilistic framework quantifies uncertainties spanning the entire fault system and extended return periods, providing comprehensive hazard characterization essential for engineering applications across diverse structural periods and urban centers.

The probabilistic component employs the OpenQuake Engine (version 3.23.1) (Global Earthquake Model Foundation, 2025b), an open-source computational platform for comprehensive seismic hazard assessment across an expanded domain encompassing the complete EAFZ system (Abrahamson et al., 2014; Pagani et al., 2014). The PSHA methodology quantifies the likelihood that ground motion at a specific location will exceed certain intensity thresholds over a given time period through the fundamental relationship :

$$\lambda(\text{IM} > im) = \sum_{i=1}^n v_i \iint P(\text{IM} > im | m, r, \theta) \cdot f_{M_i}(m) \cdot f_{R_i}(r | m) \cdot f_{\Theta_i}(\theta | m, r) dm dr d\theta \quad 1$$

where:

- $\lambda(\text{IM} > im)$  represents the annual frequency of exceedance of a ground motion intensity measure  $IM$  above a threshold value  $im$ .
- $v_i$  is the annual occurrence rate of earthquakes from source  $i$ .
- $P(\text{IM} > im | m, r, \theta)$  is the conditional probability of exceeding intensity  $im$  given magnitude  $m$ , distance  $r$ , and other variables  $\theta$ .
- $f_{M_i}(m)$ ,  $f_{R_i}(r | m)$  and  $f_{\Theta_i}(\theta | m, r)$  are probability density functions for magnitude, distance, and other parameters.

The computational architecture implements a logic tree framework comprising 162 end branches, derived from twenty-seven source model branches combined with six ground motion prediction equations. Source model development addresses multi-segment rupture potential through three distinct configuration scenarios as shown in Figure 4. Individual Segments Model

(ISM), Limited Multi-Segment Model (LMSM), and Extensive Multi-Segment Model (EMSM). The detailed source configurations for these models are provided in the supplementary materials. Magnitude-frequency relationships follow the Gutenberg-Richter formulation:

$$\log_{10} N(M) = a - bM, \quad M_{\min} \leq M \leq M_{\max}$$

2

where  $N(M)$  represents the annual rate of earthquakes exceeding magnitude  $M$ . Maximum magnitudes are estimated using (Wells & Coppersmith, 1994) empirical scaling relationships:

$$M_{\max} = 5.08 + 1.16 \log L$$

3

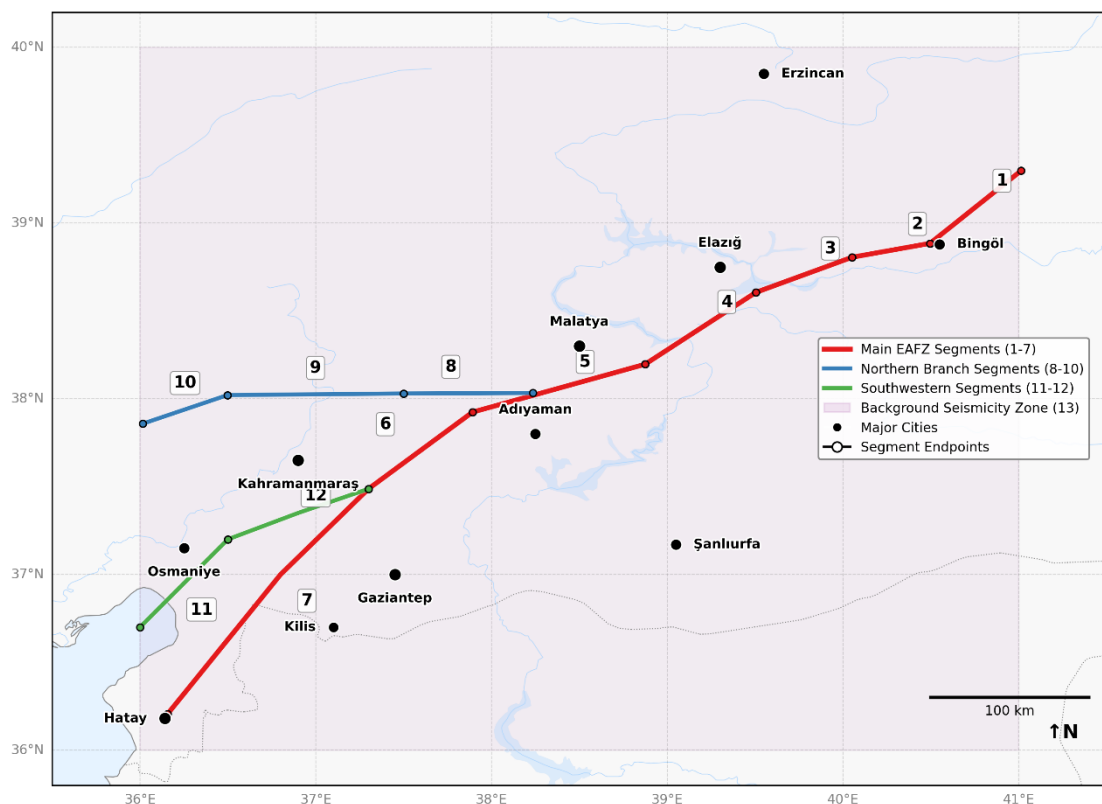


Figure 4. provides a comprehensive visualization of the fault segmentation model, illustrating the spatial distribution and geometric configuration of the thirteen primary segments (numbered 1-13) across the EAFZ region, with color-coded distinction between main faults segments and secondary structures.

where  $L$  represents surface rupture length in kilometers (Field et al., 2014; Schwartz & Coppersmith, 1984). Ground motion prediction employs a weighted ensemble of six regionally calibrated GMPEs selected based on tectonic compatibility and regional calibration (Bommer et al., 2010). The ensemble incorporates (Akkar et al., 2014) with 25% weight, reflecting comprehensive Euro-Mediterranean calibration including substantial Turkish strong-motion data; (Akkar & Cagnan, 2010) with 20% weight for direct Turkish regional applicability;

(Chiou & Youngs, 2014) with 20% weight for sophisticated directivity treatment in strike-slip environments; (Campbell & Bozorgnia, 2014) with 15% weight for detailed near-fault effects modeling; (Kotha et al., 2020) with 15% weight incorporating latest European strong-motion datasets; and (Boore & Atkinson, 2008) with 5% weight for historical reference and methodological consistency. Site response characterization employs uniform  $VS_{30} = 760$  m/s across the study region, representing typical rock site conditions, with basin depth parameters set to  $Z_{1.0} = 100$  m and  $Z_{2.5} = 500$  m based on regional geophysical constraints. Aleatory variability is captured through GMPE sigma terms, while epistemic uncertainty is addressed through the logic tree framework encompassing the complete ensemble of ground motion models.

## 2. Physics-Based Simulation Validation Framework

To establish confidence in the regional seismo-tectonic framework including velocity structure, fault geometry parameterization, and crustal properties that inform the probabilistic hazard assessment, high-resolution physics-based simulation provides validation against the comprehensively recorded 2023 Kahramanmaraş earthquake sequence. This validation demonstrates the reliability of computational modeling for the EAFZ tectonic environment and quantifies accuracy bounds across different distance ranges and geological conditions. The physics-based framework employs SPECFEM3D, a spectral-element method code optimized for wave propagation in complex three-dimensional media, implementing the validated regional framework subsequently utilized in PSHA ground motion prediction. The computational domain encompasses a  $150 \times 150 \times 50$  km<sup>3</sup> region centered on the 2023 Kahramanmaraş earthquake rupture zone, extending from surface to 50 km depth as illustrated in Figure 5. The variable-resolution mesh implements three distinct tiers: shallow crustal layers (0–0.7 km depth) utilize 100 m elements, mid-crustal layers (0.7–5 km depth) employ 300 m elements, and deep crustal layers (5–50 km depth) implement 900 m elements. This configuration yields approximately twenty-one million hexahedral elements, resulting in 2.6 billion global grid points when implemented with fifth-order spectral elements (Figure 5). Boundary conditions incorporate free-surface topography using SRTM digital elevation data, while lateral and basal boundaries employ Perfectly Matched Layer absorbing conditions to minimize artificial reflections (Festa & Vilotte, 2005).

The 13-layer velocity structure extends to 50 km depth with detailed parameters specified in Table 1. Velocity parameterization follows empirically derived relationships calibrated to Eastern Anatolian geophysical data  $V_p(z) = 900 + 400z$  and  $V_s(z) = 350 + 250z$  for

sedimentary deposits, progressing to crystalline basement properties at depth (Angus et al., 2006; Zor et al., 2003). Attenuation parameters incorporate depth-dependent quality factors with  $Q_p$  values ranging from 70 in shallow layers to 650 at depth, maintaining  $Q_s \approx Q_p/2$  throughout.

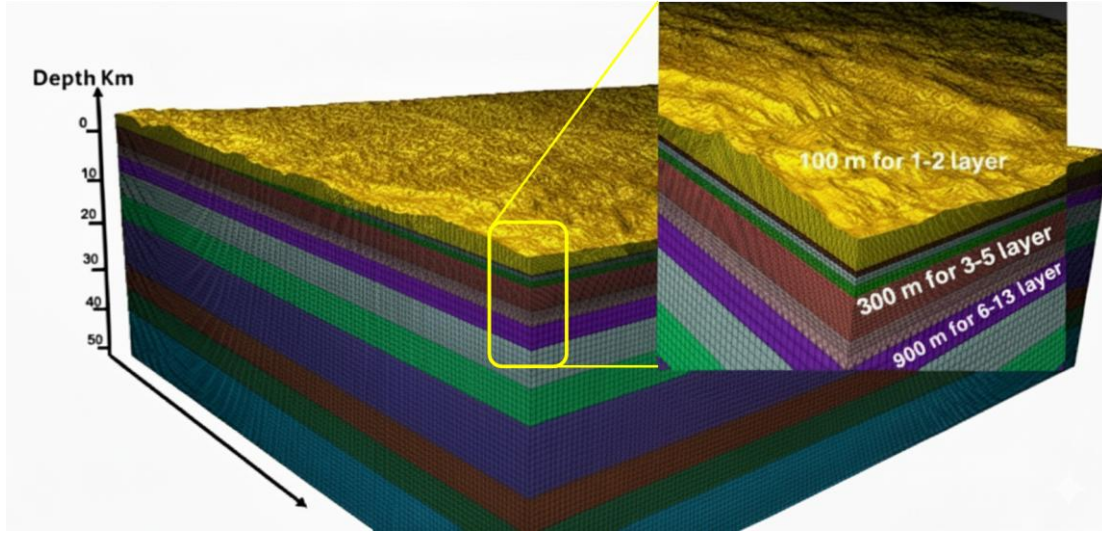


Figure 5. illustrates the variable-resolution mesh structure through a vertical cross-section, highlighting the transition between resolution tiers and the integration of surface topography.

## 2.1 Earthquake Source Characterization

The 2023 Kahramanmaraş earthquake source employs a kinematic rupture model implementing the methodology of Graves and Pitarka (2010). The hypocenter is located at 37.226°N, 37.014°E, depth 17.5 km, with focal mechanism characterized by strike = 318°, dip = 89°, rake = -179° representing predominantly left-lateral motion. Total seismic moment is  $M_0 = 5.389 \times 10^{20} \text{ N}\cdot\text{m}$  ( $M_w$  7.8). The kinematic source implementation utilizes a distributed network of 352 point sources positioned strategically along the fault planes (Figure 6). Slip velocity at each point follows:

$$\dot{D}(x, y, t) = D(x, y) \cdot V(t - t_r(x, y)) \quad 4$$

where  $D(x, y)$  represents final slip distribution,  $V(t)$  denotes the normalized slip velocity function, and  $t_r(x, y)$  is the rupture time. The slip velocity function implements an asymmetric cosine with rise time varying according to slip amplitude:

$$V(t) = \begin{cases} \frac{1}{T_r} \left[ 1 - \cos \frac{2\pi t}{T_r} \right] & \text{for } 0 \leq t \leq T_r \\ 0, & \text{otherwise} \end{cases} \quad 5$$

where  $T_r = \alpha \cdot D$ , with  $\alpha = 1.6 \text{ s/m}$  derived from empirical scaling relationships (Mai & Beroza, 2002). Rupture time is calculated as:

Table 1. Seismic Velocity Parameters for Kahramanmaraş Region

Layer	Depth Range (km)	Layer Thickness (km)	Vp (km/s)	Vs (km/s)	Density (g/cm³)	Qp	Qs
1	0–0.3	0.3	0.90	0.35	2.00	70	35
2	0.3–0.7	0.4	1.80	0.80	2.20	140	70
3	0.7–1.3	0.6	2.50	1.30	2.30	120	60
4	1.3–2	0.7	3.22	1.78	2.33	150	75
5	2–5	3	4.62	2.65	2.55	250	125
6	5–7	2	5.57	3.20	2.67	360	180
7	7–10	3	5.94	3.42	2.74	392	196
8	10–15	5	6.15	3.53	2.78	400	200
9	15–20	5	6.23	3.55	2.85	425	213
10	20–30	10	6.30	3.60	2.94	437	219
11	30–35	5	6.90	4.00	3.10	450	225
12	35–40	5	7.80	4.40	3.30	600	300
13	40–50	10	8.10	4.70	3.40	650	325

$$t_r(x, y) = \frac{r(x, y)}{V_r} \quad 6$$

where  $r(x, y)$  is distance from hypocenter and  $V_r$  is rupture velocity (2.3–3.1 km/s across segments). The kinematic rupture model incorporates complex multi-segment slip distribution characteristics derived from geodetic and seismological inversions of the 2023 Kahramanmaraş earthquake sequence (Figure 7). The fault system comprises three primary segments with distinct geometric configurations: Segment 1 (strike = 28°, dip = 85°), Segment 2 (strike = 60°, dip = 85°), and Segment 3 (strike = 25°, dip = 75°), each exhibiting systematic variations in slip amplitude and rupture propagation characteristics. Slip distribution demonstrates pronounced heterogeneity across the fault planes, with maximum slip concentrations reaching 10 meters concentrated along Segment 2 (Erkenek segment) at intermediate depths of 5–15 km. The hypocenter, denoted by the star symbol in Figure 7, initiated rupture at 17.5 km depth, with subsequent bilateral propagation exhibiting asymmetric characteristics.

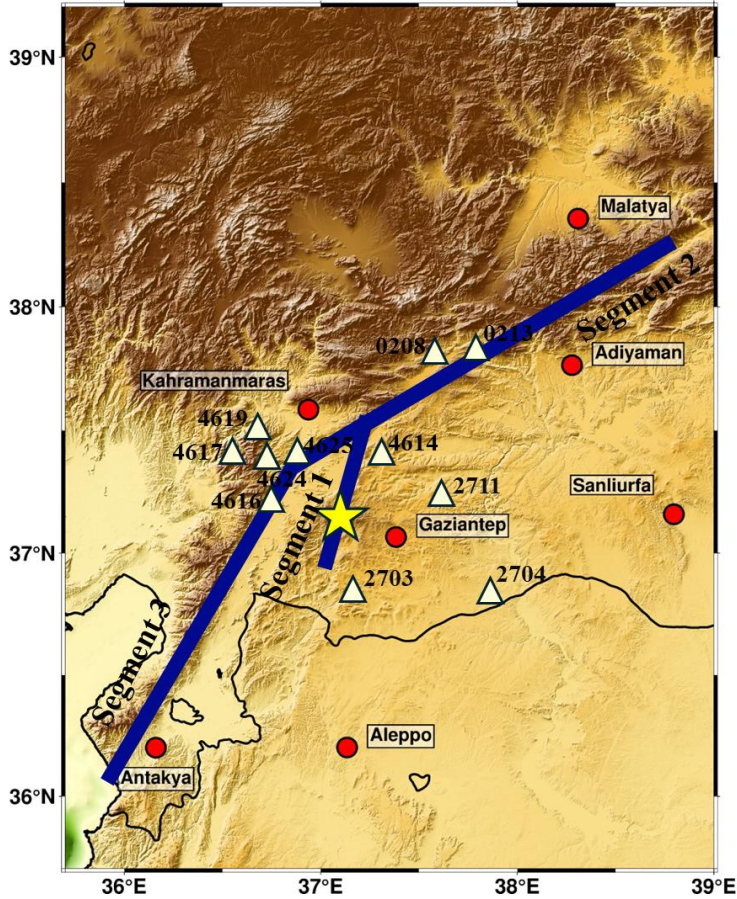


Figure 6. Topographic map of the simulation domain showing the 2023 Kahramanmaraş earthquake epicenter (yellow star), major fault segments that ruptured during the event (blue lines), strong-motion recording stations (white triangles), and major cities.

Rupture front contours, plotted at 10-second intervals, reveal systematic along-strike progression with average rupture velocities ranging from 2.3 to 3.1 km/s across different segments, consistent with sub-Rayleigh propagation velocities characteristic of continental strike-slip earthquakes. The slip vector orientations, indicated by arrows showing hanging wall motion relative to the footwall, confirm predominantly left-lateral strike-slip kinematics with rake angles approaching  $-179^\circ$ , though localized variations in rake reflect complex fault geometry at segment boundaries. Segment 1 exhibits relatively uniform but moderate slip amplitudes of 2-4 meters distributed across a compact fault plane extending approximately 40 km along strike. In contrast, Segment 2 demonstrates the most substantial moment release with slip amplitudes exceeding 10 meters concentrated in a distinct asperity zone positioned at 50-100 km along-strike distance, reflecting accumulated strain release from prolonged interseismic loading. Segment 3 presents an intermediate slip pattern with peak amplitudes of 6-8 meters distributed across an extended rupture surface of approximately 160 km length.

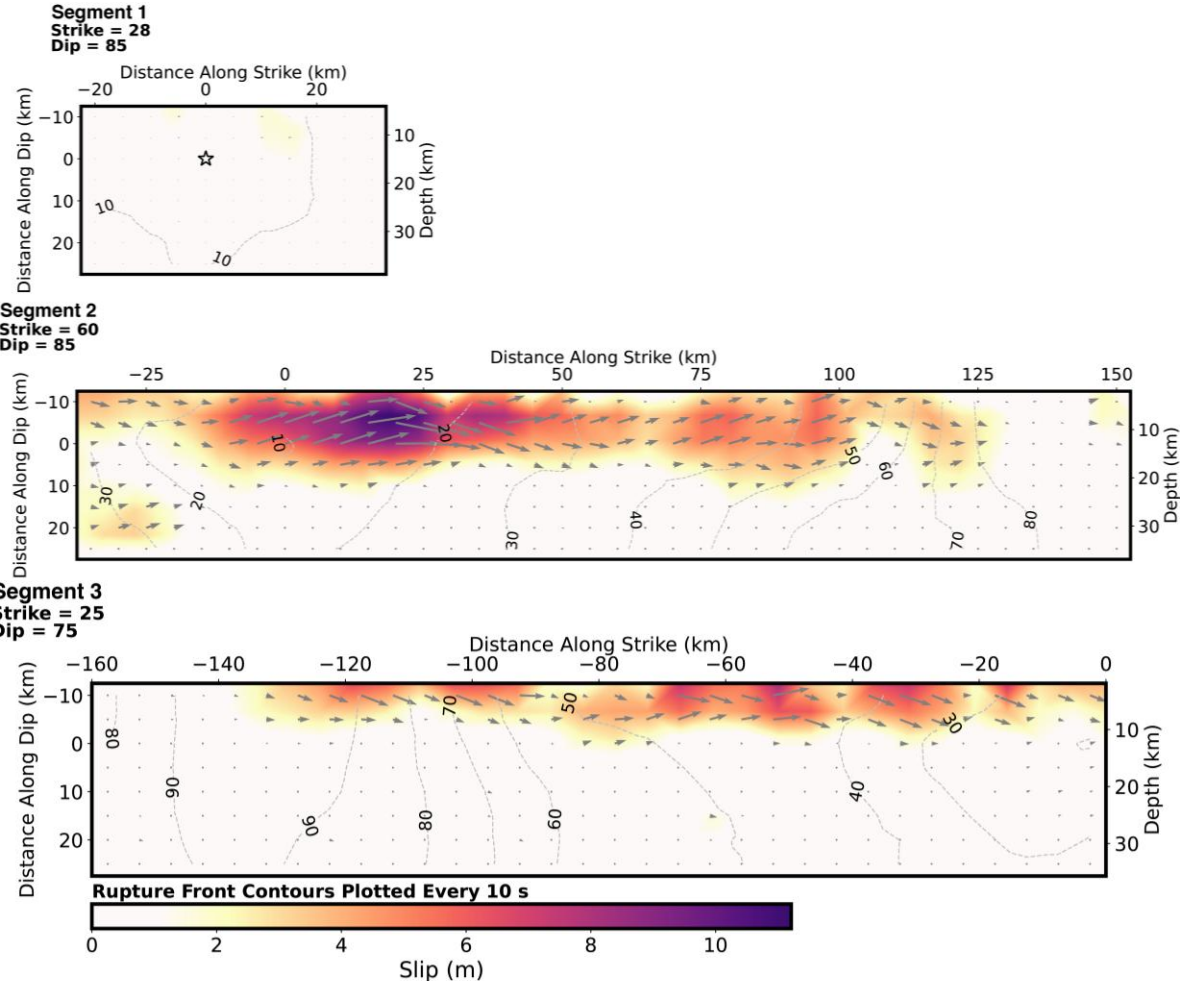


Figure 7. Cross-section of slip distribution. The strike direction is indicated above each fault plane and the hypocenter location is denoted by a star. Slip amplitude is shown in color and the motion direction of the hanging wall relative to the footwall (rake angle) is indicated with arrows. Contours show the rupture initiation time in seconds.(United States Geological Survey, 2023)

The spatial correlation between high-slip zones and rupture time contours indicates systematic complexity in the rupture process, with localized acceleration and deceleration phases governing the overall energy release characteristics. This heterogeneous slip distribution, derived from comprehensive inversion of strong-motion, geodetic, and teleseismic datasets, provides essential constraints for kinematic source parameterization and serves as the fundamental basis for physics-based ground motion simulation throughout this investigation. The source time function implements a half-cosine formulation:

$$f(t) = \frac{1}{2} \left[ 1 - \cos \frac{\pi t}{t_{\text{half}}} \right] \quad \text{for } 0 \leq t \leq 2t_{\text{half}} \quad 7$$

where  $t_{\text{half}} = 4.5$  seconds corresponding to ~9 seconds for initial peak moment release, though complete rupture extended 60–100 seconds across multiple segments.

## Probabilistic Seismic Hazard Assessment Results

Regional hazard analysis reveals distinctive spatial patterns of ground motion intensity across the fault zone. The comprehensive probabilistic seismic hazard assessment reveals distinctive spatial patterns of ground motion intensity across the East Anatolian Fault Zone, characterized by pronounced hazard concentration along the primary fault trace and systematic scaling with return period. The peak ground acceleration hazard maps (Figure 8) demonstrate a well-defined high-hazard corridor extending along the main EAFZ structure, with maximum values reaching approximately 2.0g for the longest return period examined. The 475-year return period PGA distribution (Figure 8A) exhibits a narrow zone of elevated hazard values extending from the northeastern segments near Elazığ to the southwestern termination near Hatay. Systematic hazard escalation occurs with increasing return periods, as demonstrated by comparison between the 475-year, 975-year (Figure 8B), and 2475-year (Figure 8C) scenarios.

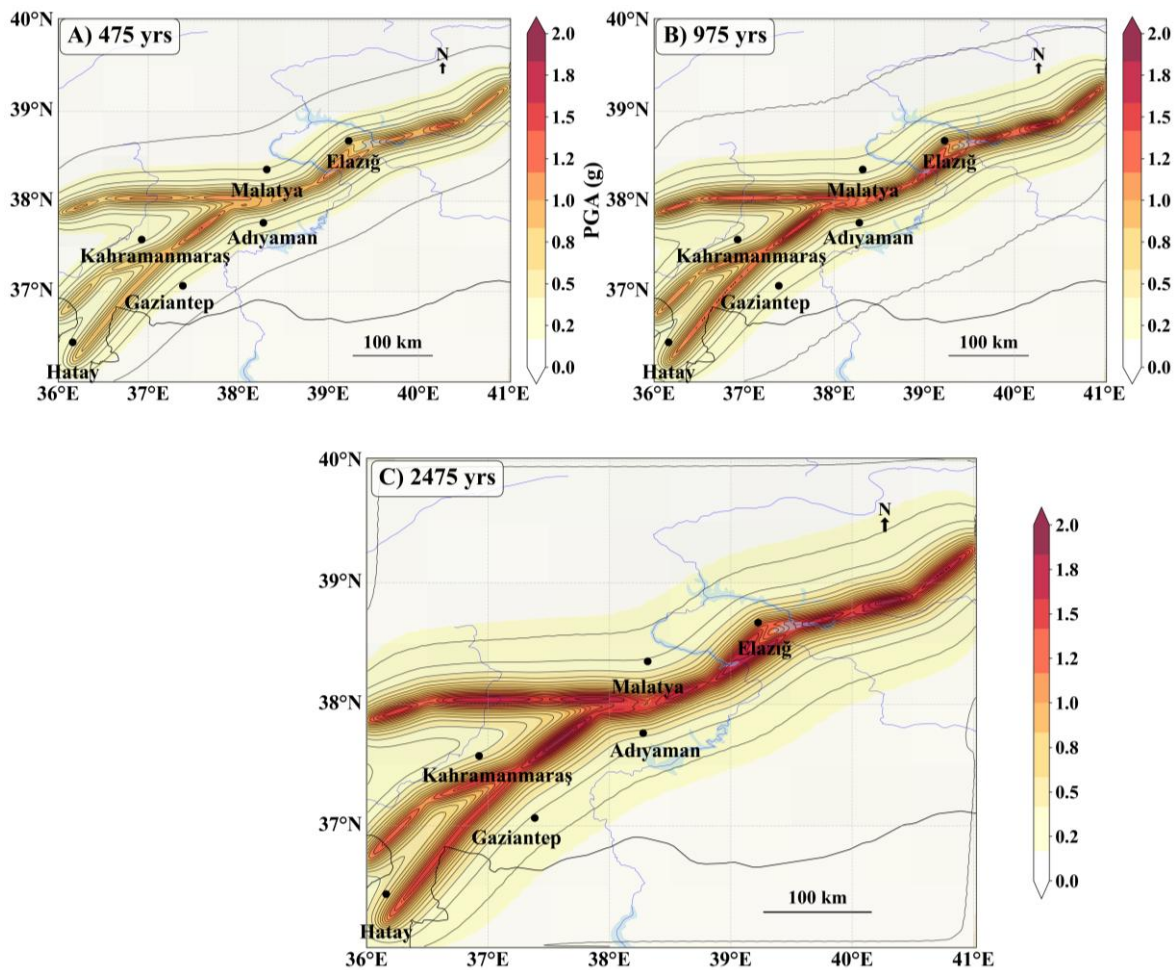


Figure 8. Peak Ground Acceleration (PGA) Hazard Maps displaying spatial distribution of ground motion intensity for return periods of (A) 475 years, (B) 975 years, and (C) 2475 years across the East Anatolian Fault Zone

Urban center exposure varies systematically based on proximity to active fault segments. Elazığ experiences the most severe seismic exposure across all return periods, positioned within the highest intensity corridor. Malatya, Adiyaman, and Kahramanmaraş exhibit intermediate hazard levels, while Gaziantep shows the lowest values among major urban centers due to its greater distance from the primary fault trace. Hatay presents substantial hazard levels, reflecting its position near the complex southwestern termination where multiple fault segments converge. The hazard levels demonstrate systematic distance-dependent attenuation, decreasing rapidly beyond 30-50 km from the primary fault trace across all return period scenarios. Spectral acceleration characteristics demonstrate period-dependent variations critical for engineering applications. The spectral acceleration hazard characterization reveals systematic period-dependent variations critical for engineering design across different structural categories. Analysis demonstrates fundamental differences in spatial patterns, amplitude scaling, and site response characteristics that govern structural vulnerability across the East Anatolian Fault Zone.

Short-period spectral accelerations (SA 0.3, **Error! Reference source not found.**) exhibit maximum hazard concentrations with values exceeding 2.2g for 2475-year return periods, representing substantial enhancement over corresponding PGA values. The distribution demonstrates sharp spatial gradients and enhanced contrast between on-fault and off-fault locations, reflecting high sensitivity to proximity-dependent high-frequency seismic energy generation. Northeastern fault segments consistently produce peak intensities, with Elazığ positioned within zones exceeding 2.0g for extended return periods. Intermediate-to-long period accelerations show progressively modified characteristics: SA(0.5s) reveals broader hazard distribution with pronounced basin amplification in sedimentary areas surrounding Kahramanmaraş, Adiyaman, and Hatay, reflecting resonance coupling between seismic waves and basin structures. SA(1.0s, Figure 10) demonstrates reduced peak amplitudes (~1.9g maximum) but significantly expanded geographic distribution with clear directivity effects through elongated contours perpendicular to fault segments. Very long-period accelerations (SA 2.0s, Figure 11) exhibit the most diffuse distribution with maximum values of 0.8g, dominated by basin amplification effects that substantially exceed those at shorter periods. Site-specific hazard evaluation quantifies systematic variations in seismic exposure among major urban centers.

The comprehensive site-specific hazard evaluation reveals systematic variations in seismic exposure that fundamentally reflects the complex interplay between fault proximity, regional seismotectonic activity, and local geological conditions across the East Anatolian

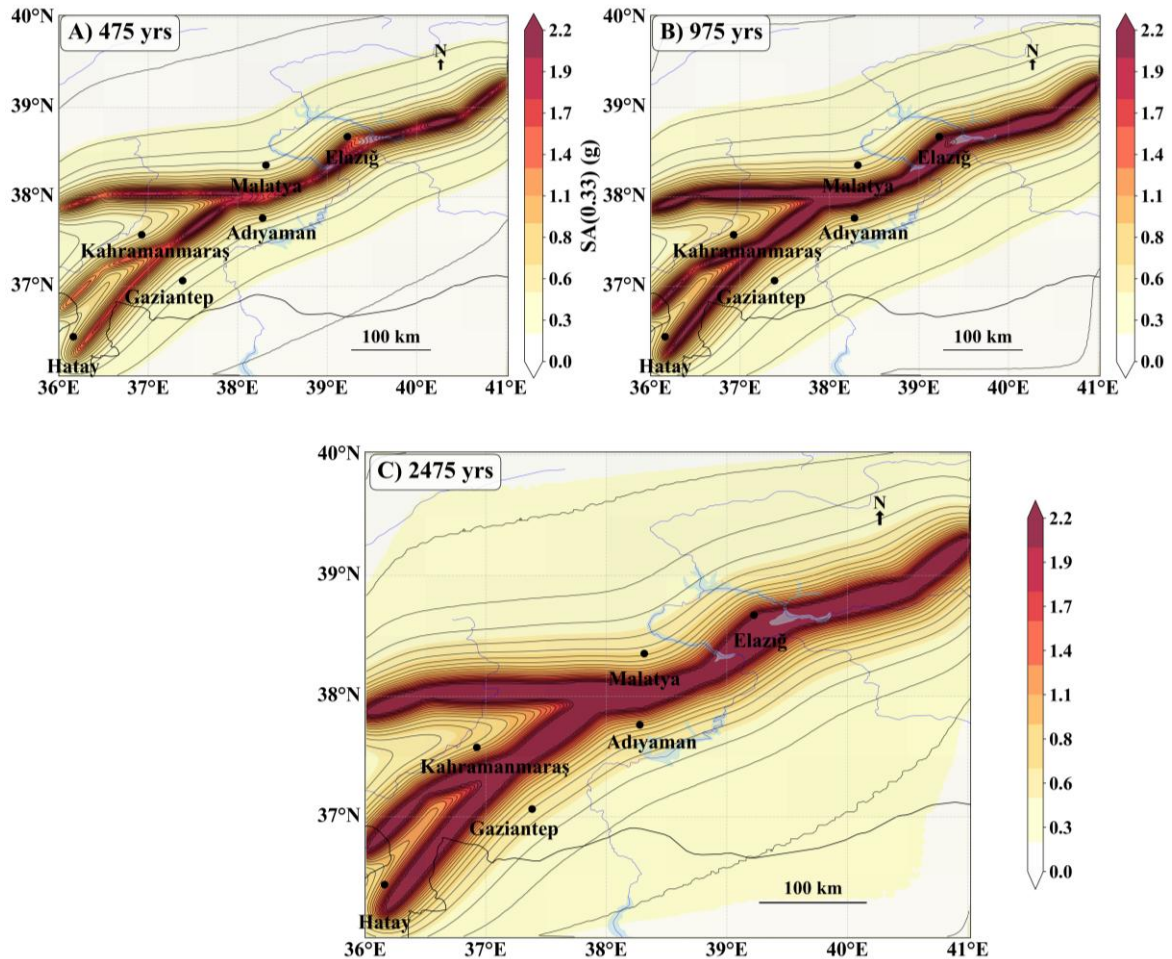


Figure 9 . Spectral Acceleration Hazard Maps at 0.3-second period showing ground motion distribution for return periods of (A) 475 years, (B) 975 years, and (C) 2475 years, particularly relevant for low-rise structural systems

Fault Zone. These variations, quantified through detailed hazard curve analysis, establish the foundation for understanding differential risk exposure among major urban centers and provide critical insights for regionally adapted seismic design strategies. Peak ground acceleration hazard curves demonstrate pronounced inter-site variability that directly correlates with proximity to active fault segments and regional tectonic activity (Figure 12).

The analysis reveals a clear tripartite classification of seismic exposure levels across the study region. High-hazard urban centers, represented by Hatay/Antakya and Elazığ, exhibit exceptionally severe ground motion exposure with 475-year design values of 0.557g and 0.567g, respectively. These values escalate dramatically to approximately 1.0g for 2475-year return periods, substantially exceeding conventional building code provisions for high seismic zones and reflecting their immediate proximity to the most seismically active northeastern and southwestern segments of the EAFZ system. In contrast, intermediate-hazard centers

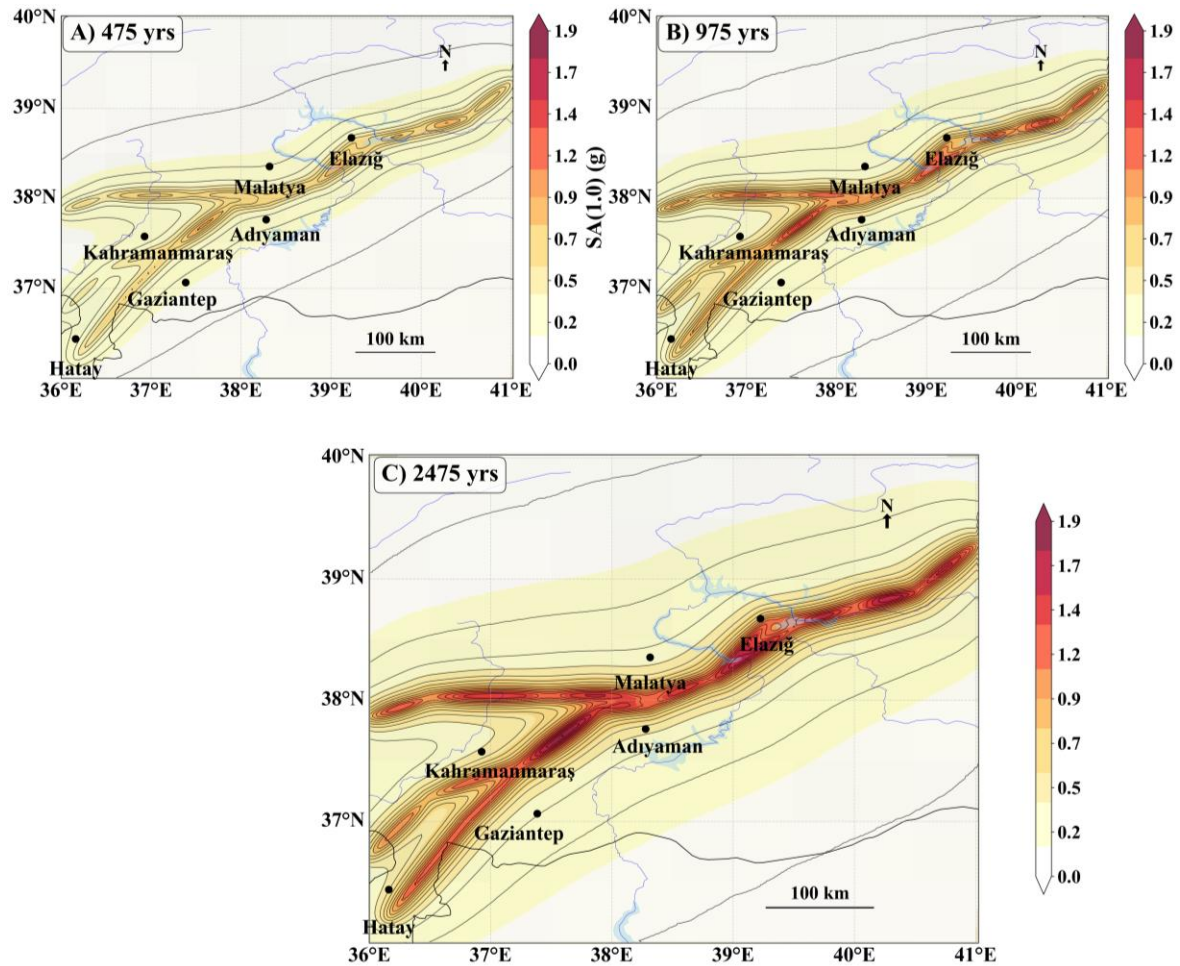


Figure 10. Spectral Acceleration Hazard Maps at 1.0-second period illustrating ground motion patterns for return periods of (A) 475 years, (B) 975 years, and (C) 2475 years, essential for tall building and long-span bridge design

demonstrate systematically reduced but nevertheless significant exposure characteristics. Kahramanmaraş and Adiyaman present 475-year design ground motions of 0.296g and 0.279g respectively, positioning these urban areas within moderate-to-high seismic exposure categories that demand comprehensive earthquake-resistant design considerations. The progression to extreme return periods reveals consistent scaling behavior, with 2475-year values reaching 0.43-0.45g. Moderate-hazard sites complete this exposure spectrum through their demonstration of comparatively conservative ground motion levels. Malatya and Gaziantep exhibits 475-year design values of 0.209g and 0.176g respectively, reflecting their greater distances from primary fault traces while nonetheless requiring substantial seismic design considerations. Significantly, all analyzed sites demonstrate remarkably uniform scaling factors ranging from 1.5 to 1.6 between 475-year and 2475-year scenarios, confirming the robustness of ground motion prediction methodologies and enabling reliable extrapolation to

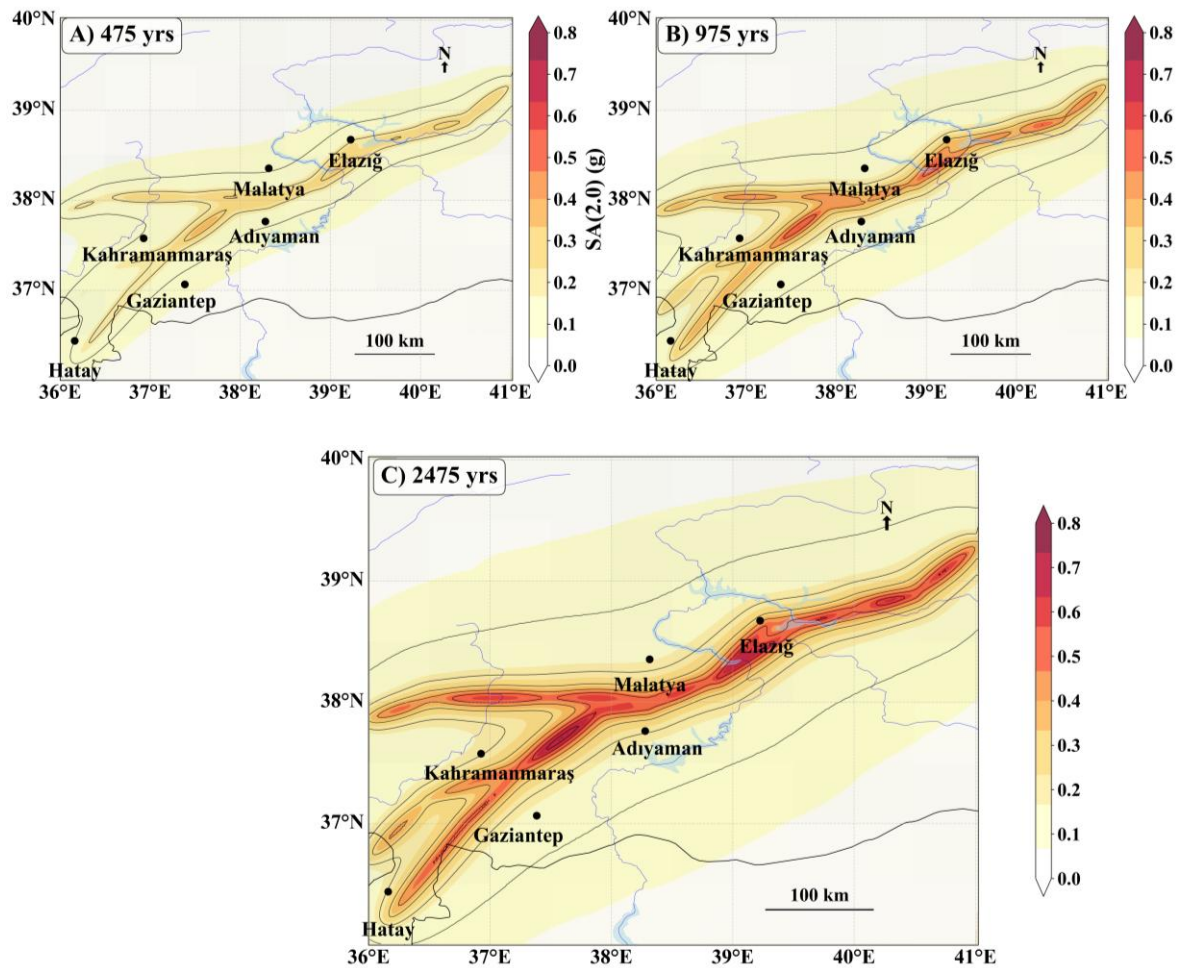


Figure 11. Spectral Acceleration Hazard Maps at 2.0-second period demonstrating ground motion characteristics for return periods of (A) 475 years, (B) 975 years, and (C) 2475 years, relevant for very flexible structural systems and base-isolated buildings

extreme event scenarios. The frequency-dependent characteristics revealed through uniform hazard spectra analysis provide essential insights into the period-specific vulnerability patterns that govern structural response across different building categories. The 475-year uniform hazard spectra (Figure 13, panel A) demonstrates systematic period-dependent amplification patterns that directly inform engineering design considerations. High-hazard sites exhibit peak spectral accelerations approaching 1.3-1.4g at 0.2-second periods, with Hatay/Antakya displaying distinctive intermediate-period enhancement reaching 0.98g at 0.5 seconds. The systematic evolution to extreme return period scenarios, illustrated through 2475-year uniform hazard spectra (Figure 13, panel B), preserves fundamental spectral shape characteristics while demonstrating proportional amplitude enhancement across all structural periods. Peak accelerations reach 2.0-2.1g for high-hazard sites and 1.1-1.2g for intermediate-hazard centers, maintaining the systematic scaling relationships observed in peak ground acceleration analysis.

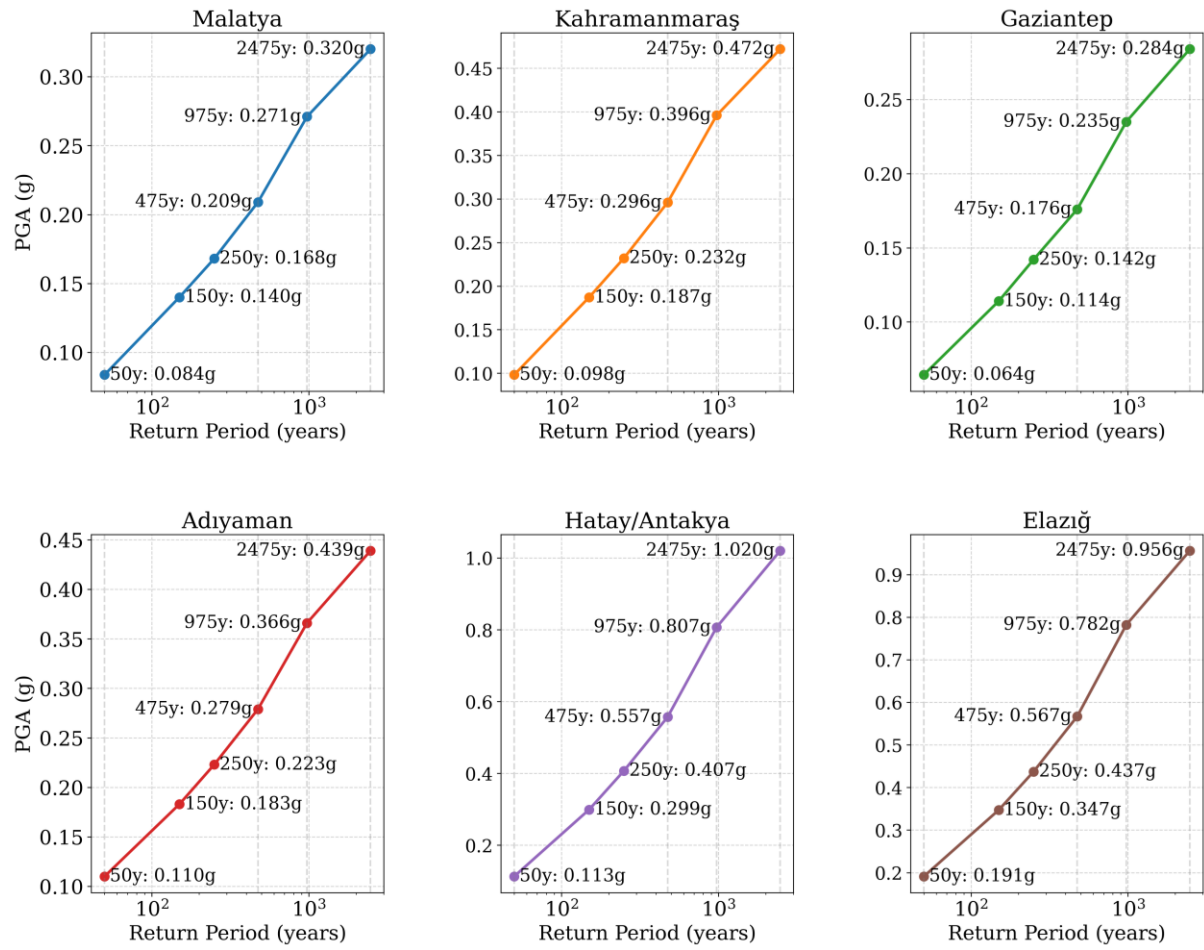


Figure 12. Peak Ground Acceleration versus Return Period for Urban Centers in the EAFZ Region, illustrating probabilistic seismic hazard curves for six major metropolitan areas with return periods spanning 50 to 2475 years, demonstrating systematic scaling relationships between ground motion intensity and exceedance probability.

The uniform scaling behavior enables reliable extrapolation to extreme event scenarios essential for critical infrastructure design.

Disaggregation analysis identifies the magnitude-distance combinations controlling ground motion exceedance probabilities. The disaggregation analysis provides fundamental insights into the magnitude-distance combinations and seismic source characteristics that control ground motion exceedance probabilities across the East Anatolian Fault Zone, enabling quantitative identification of controlling earthquake scenarios through systematic decomposition of hazard contributions across the magnitude-distance-epsilon parameter space. The comprehensive evaluation encompasses geographic hazard contribution patterns, magnitude-distance modal relationships, and three-dimensional source characterization across multiple ground motion parameters. The geographic hazard contribution analysis for the 475-

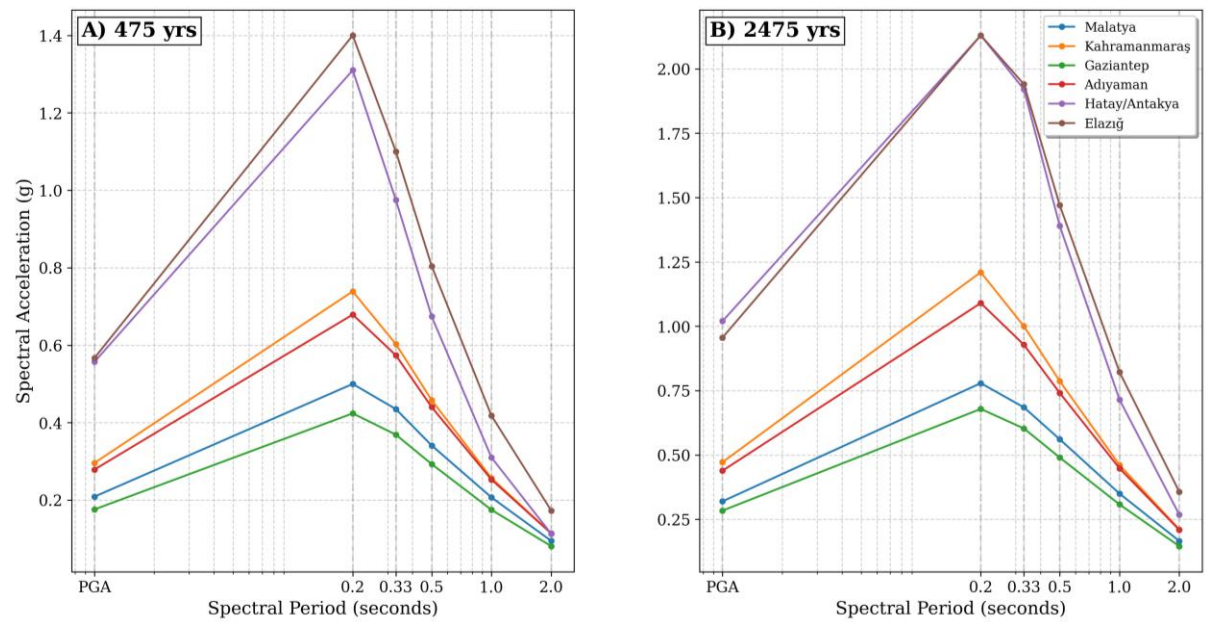


Figure 13. Uniform Hazard Spectra for Key Urban Centers at (A) 475-year and (B) 2475-year Return Period, displaying spectral acceleration characteristics across structural periods from PGA to 2.0 seconds for engineering design applications and revealing site-specific ground motion amplification patterns.

year return period reveals distinctive spatial patterns reflecting complex interactions between fault geometry, seismic source distribution, and distance attenuation relationships (Figure 14). Gaziantep exhibits the highest maximum mean hazard contribution values at 0.092g within the 50-kilometer analysis radius, despite its off-fault positioning. Malatya demonstrates substantial contributions approaching 0.088g with concentrated high-intensity zones aligning with active fault segments, while Hatay/Antakya presents values reaching 0.079g. The moderate-hazard centers exhibit systematically lower intensities, with Kahramanmaraş at 0.076g, Adıyaman at 0.072g, and Elazığ at 0.070g, demonstrating systematic scaling relationships that correspond to fault trace proximity and regional seismotectonic activity patterns. The evolution to 2475-year return period scenarios demonstrates modified contribution patterns emphasizing enhanced influence of distant, high-magnitude sources on extreme ground motion generation (Figure 15). Maximum mean hazard contributions show systematic reduction with Hatay/Antakya reaching 0.018g, Gaziantep maintaining elevated levels at 0.016g, and Kahramanmaraş exhibiting 0.015g, while remaining centers demonstrate values ranging from 0.012g. The magnitude-distance disaggregation analysis reveals controlling earthquake scenarios that drive design-level ground motion exposure through systematic site-specific patterns reflecting proximity to active fault segments and regional geological conditions (Figure 16).

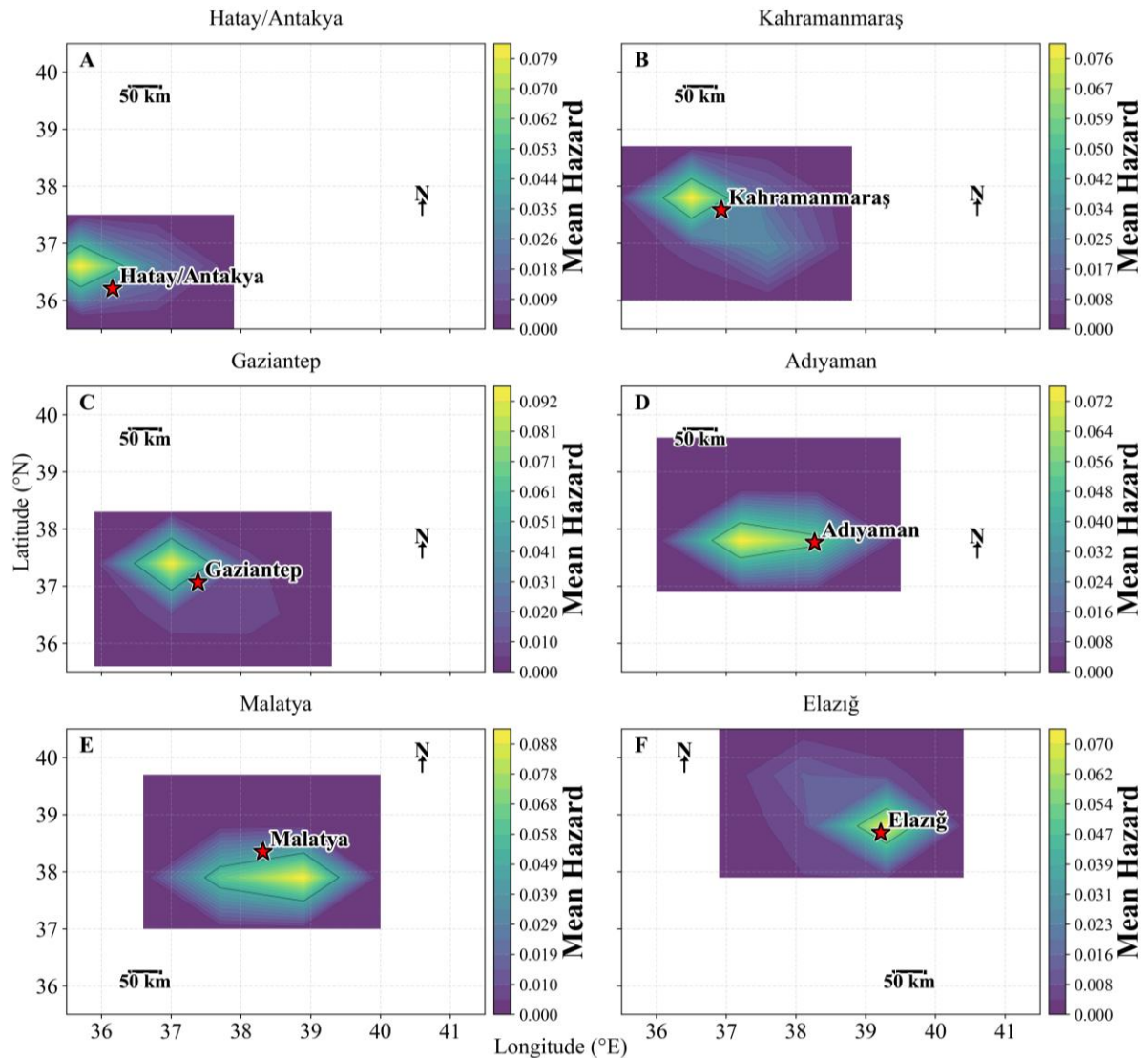


Figure 14. Geographic Hazard Contribution Comparison Across All Sites for 475-year Return Period PGA, illustrating spatial distribution of seismic hazard contributions within 50-kilometer radius zones surrounding each major urban center, with color-coded mean hazard intensities reflecting source proximity and activity levels.

Kahramanmaraş demonstrates the most severe near-source hazard characteristics with modal scenario parameters of Mw6.8 at 5km distance and mean parameters of Mw6.3 at 7km, indicating dominance by large-magnitude, proximal earthquake scenarios reflecting immediate proximity to active EAFZ segments. Conversely, Gaziantep exhibits controlling scenarios characterized by modal parameters of Mw6.8 at 65km and mean parameters of Mw6.4 at 59km, reflecting off-fault positioning and consequent dependence on distant seismic sources for significant ground motion generation.

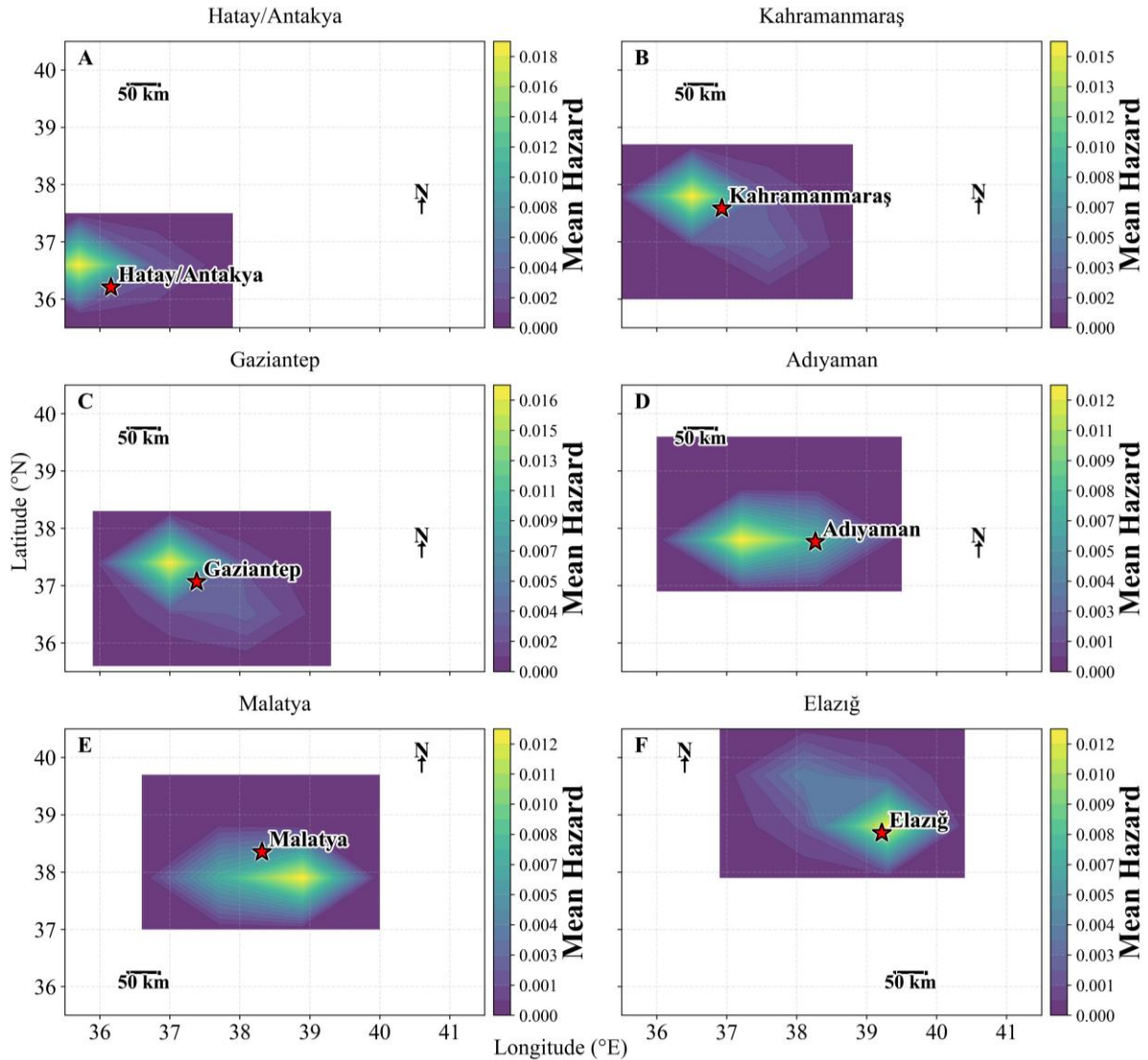


Figure 15. Geographic Hazard Contribution Comparison Across All Sites for 2475-year Return Period PGA, demonstrating enhanced spatial resolution of seismic source contributions for extreme return periods with modified color scaling reflecting increased contribution from rare, high-magnitude earthquake scenarios.

The northeastern centers demonstrate contrasting patterns, with Elazığ exhibiting modal parameters of Mw6.8 at 85km and mean parameters of Mw6.1 at 66km despite fault-adjacent location, while Malatya shows distinctive characteristics with modal parameters of Mw5.8 at 15km and mean parameters of Mw6.0 at 11km, representing the lowest magnitude controlling scenarios while maintaining near-source distance characteristics. The systematic evolution toward 2475-year controlling scenarios demonstrates magnitude enhancement while preserving site-specific distance characteristics (Figure 17). Kahramanmaraş maintains near-source dominance with enhanced magnitude contributions reaching modal parameters of Mw6.8 at 5km and mean parameters of Mw6.5 at 5km, while Gaziantep preserves distant-

source dependence with modal parameters of Mw6.8 at 55km and mean parameters of Mw6.3 at 46km. Notably, Elazığ exhibits dramatic disaggregation evolution with modal parameters shifting to Mw5.2 at 15km and mean parameters of Mw5.7 at 34km, representing substantial reduction in both magnitude and distance for extreme controlling scenarios.

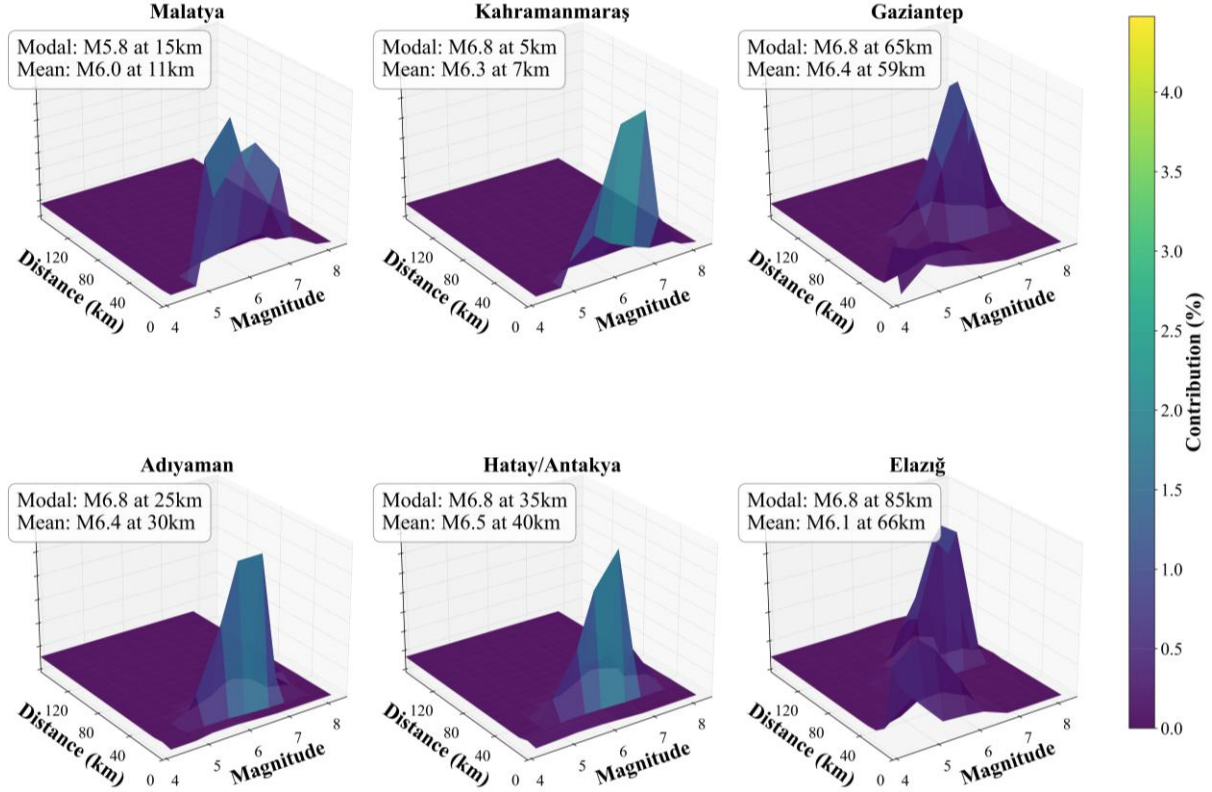


Figure 16. Magnitude-Distance Disaggregation for 475-year Return Period PGA, displaying three-dimensional surface representations of the joint magnitude-distance probability distributions that control design-level ground motions, with modal and mean scenario parameters quantified for each urban center.

The spectral acceleration disaggregation demonstrates systematic period-dependent modifications in controlling scenarios that directly inform frequency-specific design considerations. Short-period spectral acceleration (SA 0.2s) maintains close correspondence with PGA characteristics, with Kahramanmaraş preserving modal parameters of Mw6.8 at 5km and mean parameters of Mw6.3 at 7km, demonstrating consistency reflecting similar frequency content characteristics of these ground motion parameters (Figure 18). The intermediate-period spectral acceleration (SA 1.0s) reveals enhanced distance sensitivity and modified controlling scenario characteristics, with Gaziantep exhibiting substantial period-dependent modifications reaching modal parameters of Mw6.8 at 75km and mean parameters of Mw6.7 at 76km (Figure 19). Elazığ demonstrates dramatic scenario evolution with modal parameters of Mw6.8 at 95km and mean parameters of Mw6.7 at 107km, representing substantial distance increases for intermediate-period controlling scenarios. The three-dimensional magnitude-

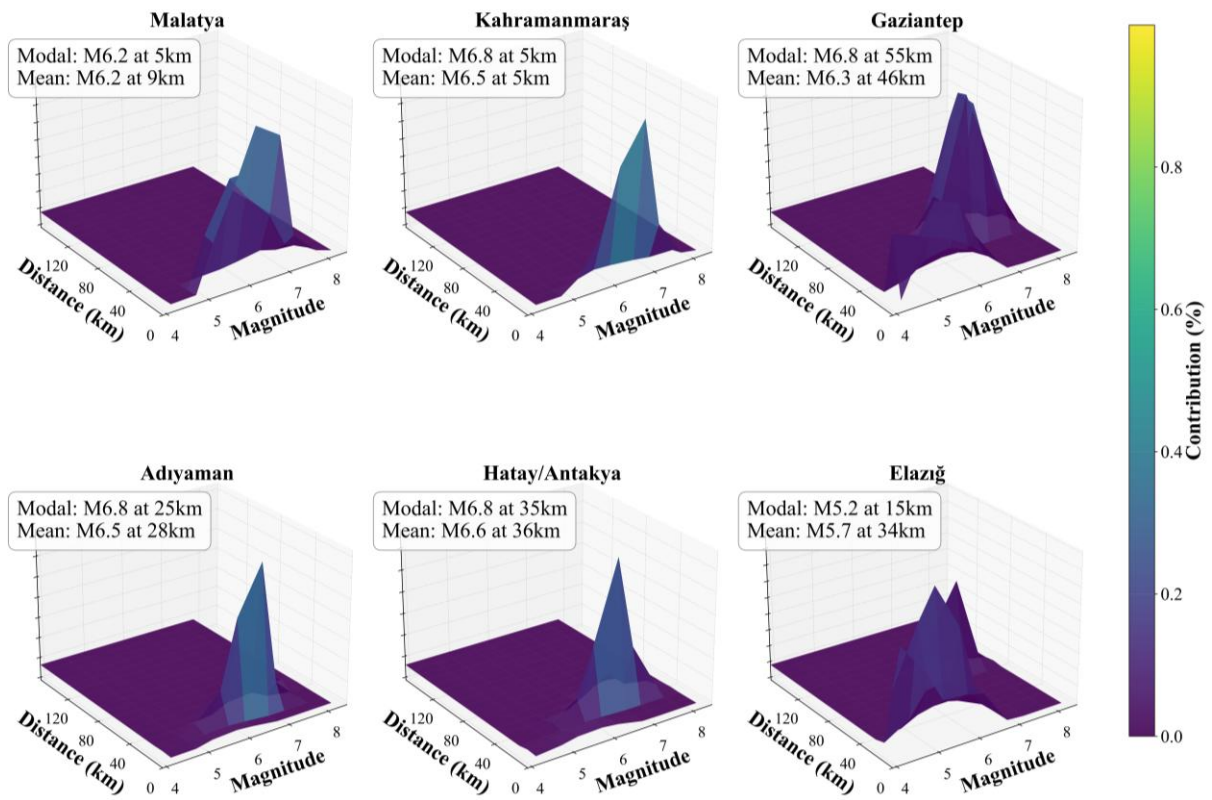


Figure 17. Magnitude-Distance Disaggregation for 2475-year Return Period PGA, illustrating the evolution of controlling earthquake scenarios for extreme return periods with enhanced emphasis on maximum magnitude events and modified distance relationships governing rare ground motion exceedance.

distance-epsilon disaggregation provides comprehensive understanding of the complete parameter space controlling ground motion exceedance probabilities, with epsilon representing standard deviations above median ground motion predictions (Figure 20-Figure 21). The 475-year analysis demonstrates concentrated epsilon distributions around modal magnitude-distance combinations for high-hazard sites, indicating that design-level ground motions are achieved through median-level earthquake scenarios rather than requiring extreme residual contributions from ground motion prediction equation uncertainties. The evolution to 2475-year scenarios demonstrates enhanced residual contributions across all sites, reflecting increasing importance of ground motion prediction equation uncertainties in generating extreme return period scenarios, with three-dimensional visualization revealing complex interaction effects between magnitude, distance, and epsilon parameters that govern rare event characteristics and inform extreme ground motion scenario development. Near-source urban centers demonstrate control by proximal, large-magnitude scenarios while off-fault locations

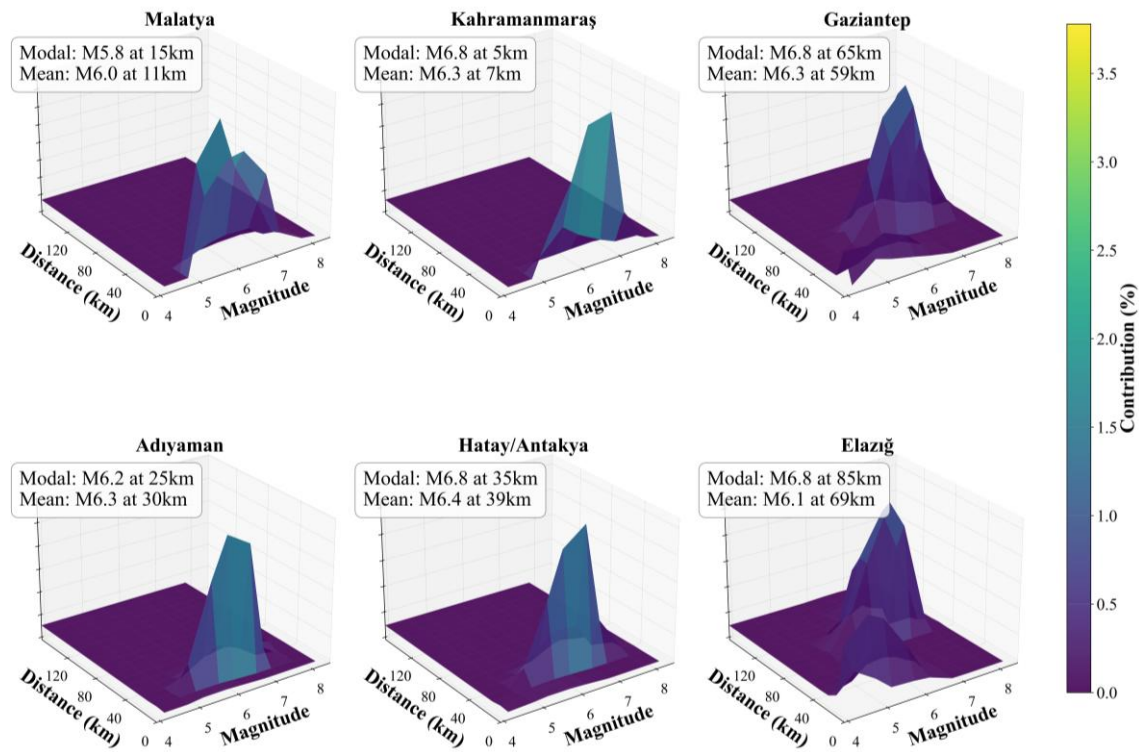


Figure 18. Magnitude-Distance Disaggregation for 475-year Return Period SA(0.2s), demonstrating spectral period-dependent variations in controlling earthquake scenarios with implications for low-rise structural design and short-period ground motion characteristics

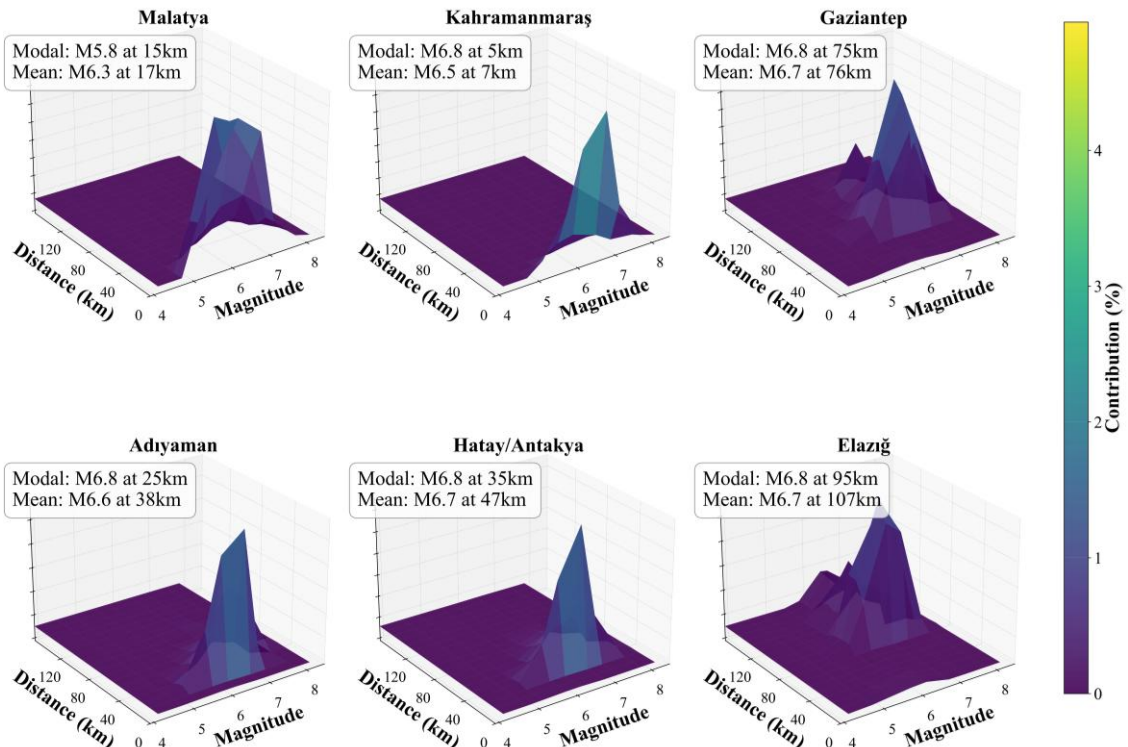


Figure 19. Magnitude-Distance Disaggregation for 475-year Return Period SA(1.0s), illustrating period-dependent evolution of controlling scenarios toward enhanced distance sensitivity and modified magnitude-distance relationships characteristic of intermediate-period ground motion generation.

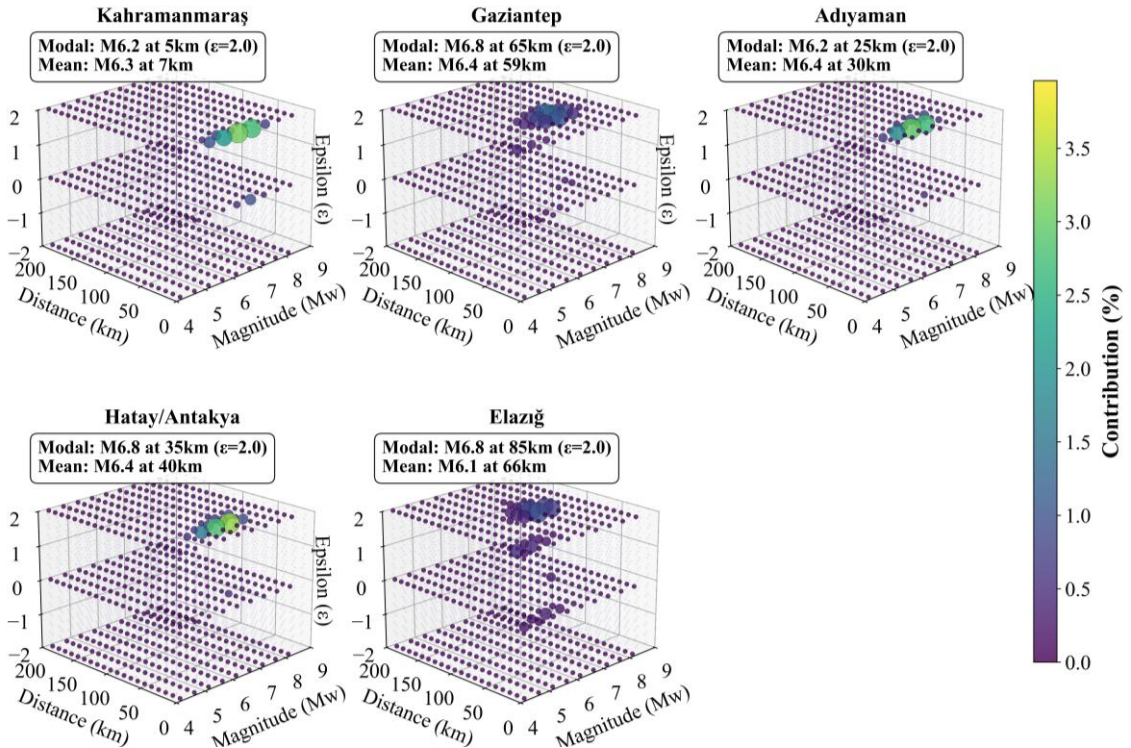


Figure 20. Three-Dimensional Magnitude-Distance-Epsilon Space Comparison for 475-year Return Period PGA, providing comprehensive visualization of the complete disaggregation space including epsilon (residual) contributions that characterize the deviation from median ground motion prediction relationships.

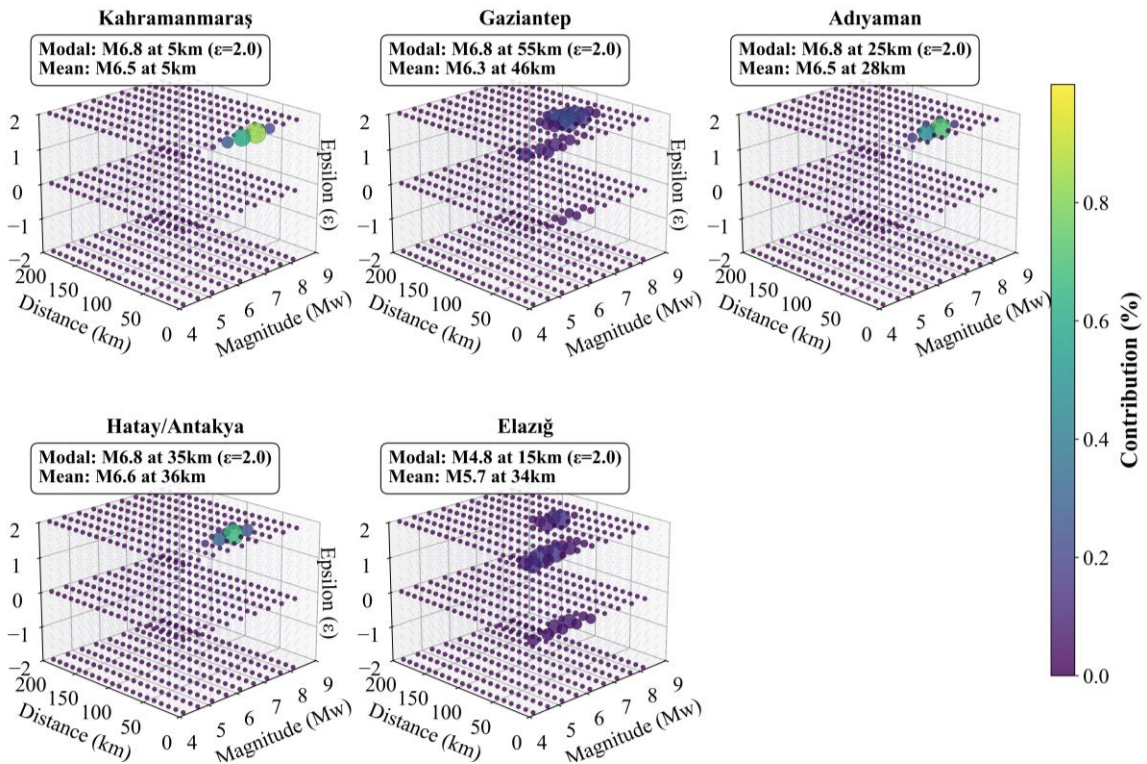


Figure 21. Three-Dimensional Magnitude-Distance-Epsilon Space Comparison for 2475-year Return Period PGA, demonstrating the evolution of three-dimensional disaggregation characteristics for extreme

return periods with enhanced epsilon contributions reflecting increased reliance on ground motion prediction equation residuals.

depend on distant, high-magnitude events. Additional comprehensive disaggregation analyses available in supplementary materials encompass 975-year return period geographic hazard contributions, magnitude-distance disaggregation for intermediate scenarios, and spectral acceleration disaggregation for SA(0.5s) and SA(2.0s) periods, providing complete frequency-dependent controlling scenario characterization across the engineering interest spectrum for comprehensive seismic risk assessment applications.

## Physics-Based Simulation Results

The physics-based simulation framework described in methodology Section 2 was systematically validated against strong-motion recordings from the 2023 Kahramanmaraş earthquake sequence to establish quantitative reliability benchmarks and identify optimal application domains for the regional seismo-tectonic framework employed throughout this investigation. This comprehensive validation provides essential confidence bounds for the velocity structure, fault geometry parameterization, and computational modeling approaches that inform the probabilistic hazard assessment. The validation analysis encompasses acceleration response spectra, velocity waveform comparisons, and systematic performance evaluation across varying distance ranges and geological conditions (Figure 22). The filtered acceleration records focus on engineering-relevant frequency content while eliminating long-period drift and high-frequency noise contamination, enabling direct comparison with design spectrum applications critical for structural engineering assessments.

The validation framework demonstrates exceptional performance characteristics at intermediate distances (20-80 km), where synthetic predictions achieve synthetic-to-observed amplitude ratios within 0.8-1.2 across all components. This optimal performance domain reflects the balance between sufficient signal strength for reliable analysis and reduced complexity from near-source effects that challenge kinematic source implementation. Near-fault environments present the most demanding validation conditions, where systematic amplitude underestimation of 25-35% underestimation reflects kinematic source limitations in kinematic source parameterization for complex rupture processes. This underestimation pattern emerges consistently across multiple components and monitoring locations, indicating fundamental challenges in reproducing high-frequency radiation patterns and directivity effects characteristic of strike-slip ruptures in close proximity to fault zones. The velocity waveform

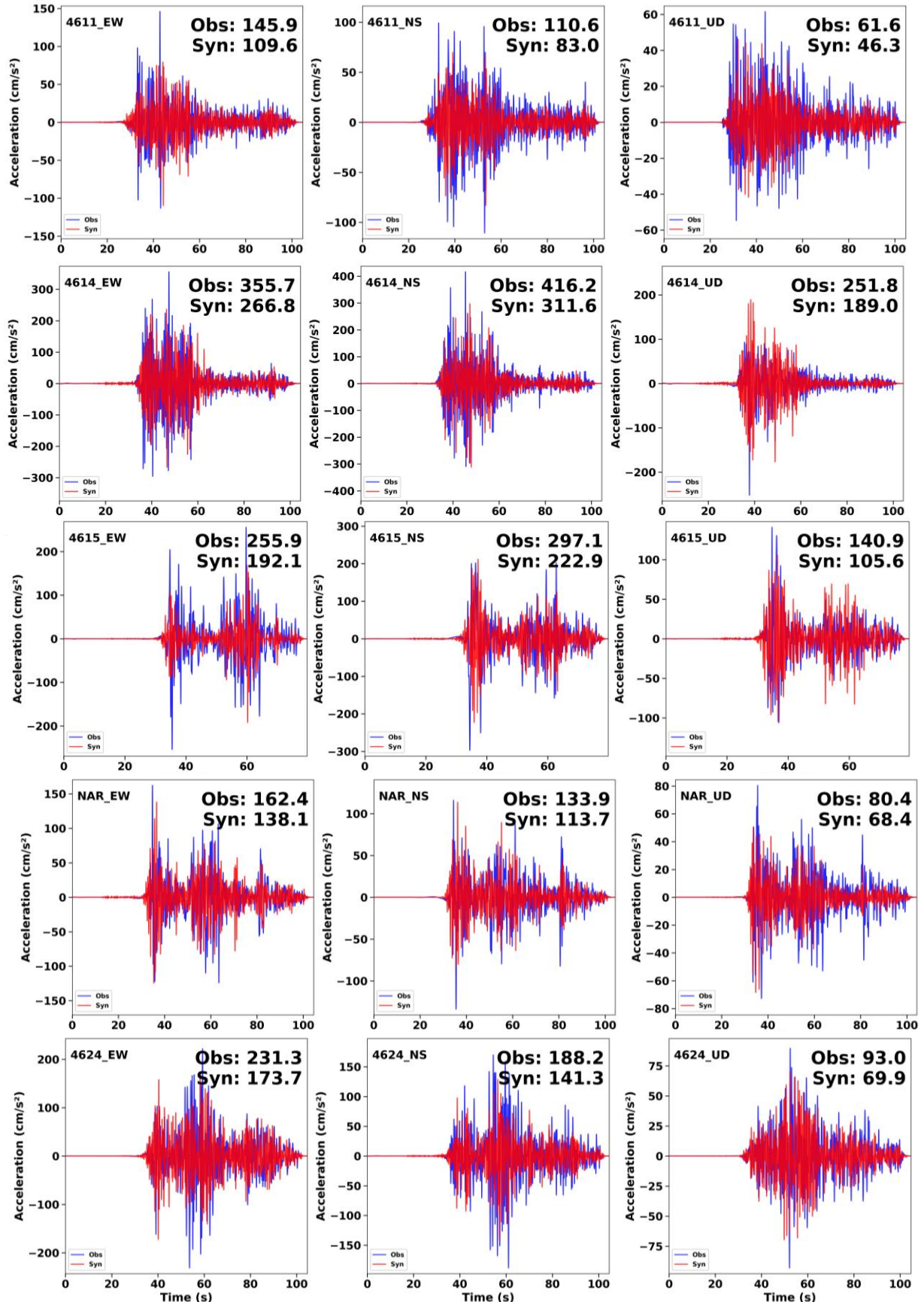


Figure 22. Time-Domain Acceleration Waveforms: Observed vs. Synthetic Ground Motion During the 2023 Mw7.8 Türkiye Earthquake.

comparison analysis provides complementary validation through zero pre-event processing with maximum amplitude scaling, effectively isolating fundamental wave propagation characteristics from noise contamination (Figure 23). The three-component velocity comparisons demonstrate exceptional fidelity in capturing primary wave arrivals, secondary phase characteristics, and overall waveform morphology across varying distance ranges.

The sustained high-frequency content preservation throughout extended analysis windows validates the velocity structure parameterization and attenuation modeling approaches employed in the numerical framework. Far-field validation establishes benchmark performance with amplitude differences consistently within 10-15% while maintaining superior waveform correlation across all components. The optimal validation domain at intermediate distances represents conditions where source complexity effects diminish while maintaining sufficient signal strength for reliable analysis, establishing this range as the primary application zone for current kinematic source implementations. Complex geological environments demonstrate consistent intermediate-distance performance characteristics, validating the 13-layer velocity structure model and its capacity to capture fundamental impedance contrasts governing seismic wave propagation. The preservation of amplitude relationships across varying geological conditions establishes confidence in the regional velocity structure parameterization while highlighting the importance of accurate subsurface characterization for numerical modeling applications. The preservation of amplitude and phase relationships establishes quantitative bounds for simulation reliability across different application domains. The physics-based simulation framework demonstrates exceptional capability for regional ground motion prediction while revealing systematic limitations that inform future methodological developments and appropriate application strategies for continental transform fault systems.

## Discussion

This investigation presents a comprehensive probabilistic seismic hazard assessment for the East Anatolian Fault Zone incorporating systematic treatment of multi-segment rupture potential, with physics-based simulation validation against the unprecedented observational dataset from the February 6, 2023, Mw 7.8 Kahramanmaraş earthquake sequence. The results fundamentally advance understanding of seismic hazard characteristics across complex continental transform systems while establishing quantitative frameworks for addressing demonstrated cascading failure mechanisms in regional hazard assessment applications.

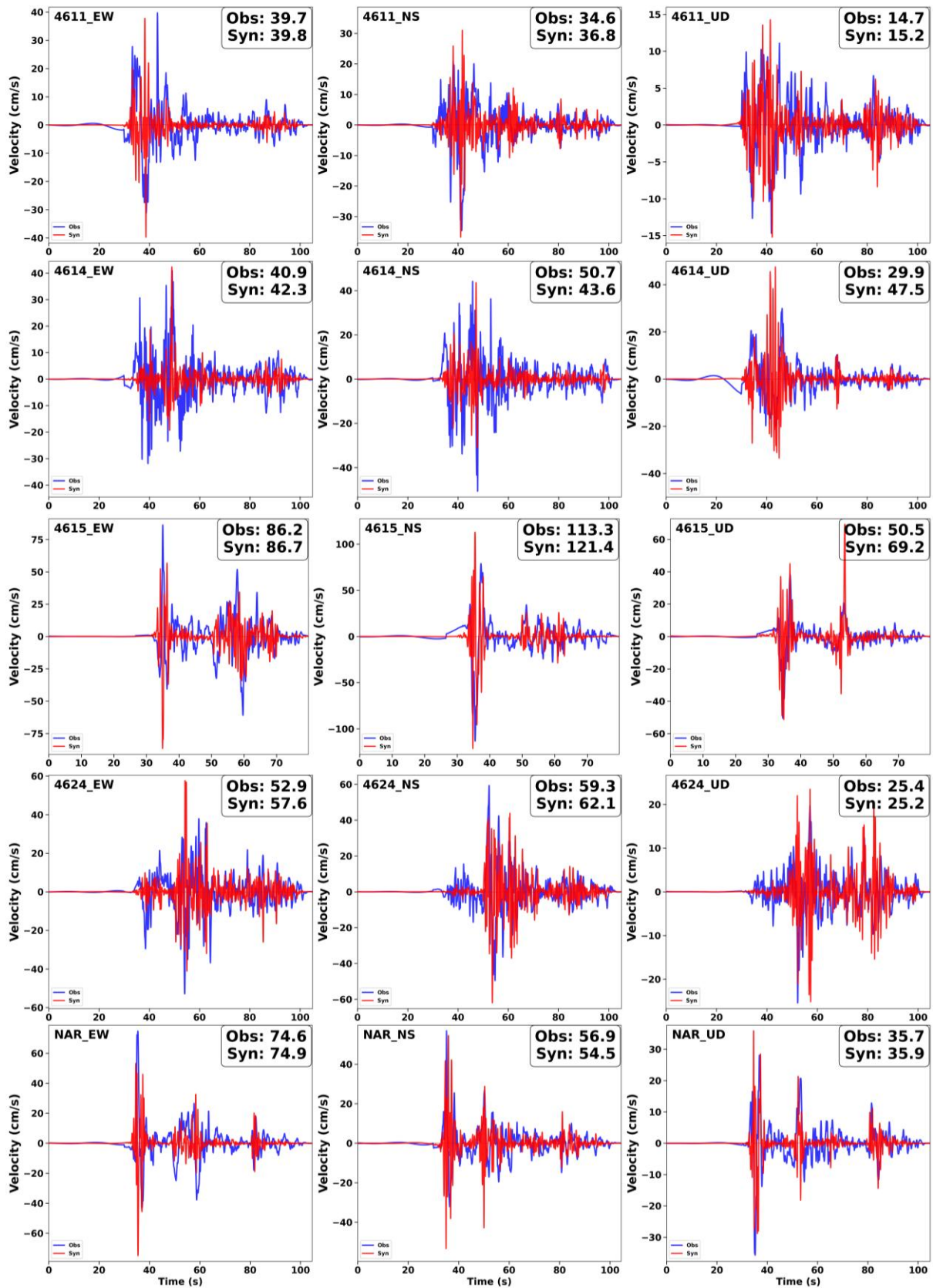


Figure 23. Temporal Evolution of Velocity Waveforms: Observed vs. Synthetic Ground Motion During the 2023 Mw7.8 Türkiye Earthquake.

The comprehensive probabilistic seismic hazard assessment represents a substantial methodological advancement through systematic treatment of multi-segment rupture scenarios that address the cascading failure potential demonstrated by the 2023 earthquake sequence. The novel source model configurations (ISM, LMSM, EMSM) provide quantitative frameworks for treating fault segments as interconnected components rather than independent seismic sources, fundamentally challenging conventional segmentation paradigms that have dominated seismic hazard practice. The 370 km surface rupture spanning multiple traditional segment boundaries during the Kahramanmaraş event validates this approach while demonstrating critical importance of considering multi-segment failure potential in complex fault systems. The logic tree framework encompassing 162 branches provides comprehensive treatment of epistemic uncertainties through systematic combination of source model variations and regionally calibrated ground motion prediction equations, advancing uncertainty quantification methodologies for continental transform environments.

Regional hazard distribution analysis reveals pronounced spatial variations that directly correlate with fault proximity and complex structural architecture, with maximum peak ground acceleration values approaching 2.0g for 2475-year return periods concentrated along a well-defined high-hazard corridor. The systematic distance-dependent attenuation relationships demonstrate consistency with established ground motion prediction models while revealing enhanced amplification characteristics in sedimentary basin environments surrounding major urban centers. The site-specific hazard assessment for Elazığ and Hatay/Antakya, revealing 475-year design values of 0.567g and 0.557g respectively, substantially exceeds conventional building code provisions and necessitates comprehensive reevaluation of seismic design criteria throughout the region. These values approach or exceed those reported for other major continental transform systems, including the San Andreas Fault Zone in California (Field et al., 2014) and the Alpine Fault in New Zealand (Stirling et al., 2012), positioning the EAFZ among the most seismically hazardous continental fault systems globally.

The spectral acceleration characterization demonstrates systematic period-dependent variations critical for engineering design across different structural categories, with short-period accelerations (SA 0.3s) exhibiting maximum values exceeding 2.2g while longer periods show progressively modified spatial patterns reflecting basin amplification effects. The intermediate-period enhancement observed at sedimentary sites, particularly around Kahramanmaraş and Hatay, demonstrates clear resonance coupling between seismic waves and basin structures that significantly amplifies ground motion exposure for mid-rise buildings and flexible infrastructure. These findings align with observations from other basin-influenced

seismic environments (Kawase, 1996; Olsen, 2000), while providing quantitative frameworks for period-specific design considerations essential for comprehensive seismic risk assessment.

The comprehensive disaggregation analysis provides fundamental insights into controlling earthquake scenarios that drive design-level ground motion exposure, revealing systematic site-specific patterns reflecting proximity to active fault segments and regional geological conditions. Near-source urban centers demonstrate control by proximal, large-magnitude scenarios (Kahramanmaraş: Mw6.8 at 5km), while off-fault locations depend on distant, high-magnitude events (Gaziantep: Mw6.8 at 65km), establishing clear relationships between fault proximity and controlling scenario characteristics. The three-dimensional magnitude-distance-epsilon analysis demonstrates that design-level ground motions are achieved through median-level earthquake scenarios rather than requiring extreme residual contributions, with systematic evolution toward enhanced residual contributions for extreme return periods reflecting increasing importance of ground motion prediction equation uncertainties in rare event generation.

The physics-based simulation validation framework demonstrates variable performance across different distance ranges and ground motion parameters, with systematic patterns emerging from comprehensive comparison against strong-motion recordings. For velocity waveforms, the simulations achieve exceptional accuracy at several stations, with Station 4611 showing remarkable agreement across all components (East-West: 39.7 vs 39.8 cm/s, North-South: 34.6 vs 36.8 cm/s, Up-Down: 14.7 vs 15.2 cm/s) and Station NAR demonstrating similar fidelity (East-West: 74.6 vs 74.9 cm/s, North-South: 56.9 vs 54.5 cm/s, Up-Down: 35.7 vs 35.9 cm/s). However, acceleration records reveal more significant discrepancies, particularly for near-fault stations where systematic amplitude underestimation is evident. Station 4614 exhibits substantial underestimation in peak ground acceleration with observed values of 355.7, 416.2, and 251.8 cm/s<sup>2</sup> compared to synthetic predictions of 266.8, 311.6, and 189.0 cm/s<sup>2</sup> respectively, representing deficits of 25-30% across components. Similarly, Station 4615 shows consistent underestimation patterns (255.9 vs 192.1 cm/s<sup>2</sup> for East-West component), reflecting fundamental challenges in kinematic source parameterization for complex high-frequency radiation patterns characteristic of strike-slip ruptures. These limitations are consistent with findings from previous continental transform system studies (Graves & Pitarka, 2016; Taborda & Bielak, 2014), indicating that dynamic rupture modeling may be necessary to adequately capture near-fault ground motion generation processes. This validation establishes confidence in the regional seismo-tectonic framework employed in the probabilistic

assessment while identifying optimal application domains where kinematic approaches provide reliable ground motion characterization.

Despite the comprehensive nature of this investigation, several methodological limitations warrant acknowledgment and inform future research directions. The physics-based simulation framework demonstrates systematic limitations in near-fault environments where kinematic source implementation inadequately reproduces complex high-frequency radiation patterns and directivity effects. The velocity structure parameterization, while incorporating regional geophysical constraints, necessarily represents simplified approximations of actual crustal heterogeneities, with uniform VS30 characterization not capturing local site amplification effects that significantly influence ground motion characteristics. The logic tree framework provides comprehensive treatment of epistemic uncertainties while necessarily simplifying complex interactions between fault system behavior and ground motion generation, with time-independent seismicity assumptions not capturing temporal clustering and stress transfer effects demonstrated by the 2023 earthquake sequence. Additionally, the assumption of uniform site conditions (VS30 = 760 m/s) across the study region may underestimate hazard variability at basin sites where significant amplification occurs.

The findings carry profound implications for seismic design practice and regulatory frameworks across the Eastern Mediterranean region, with systematic exceedance of conventional building code provisions at high-hazard urban centers necessitating comprehensive reevaluation of seismic design criteria. The period-dependent hazard characteristics provide essential foundations for frequency-specific design considerations, particularly highlighting enhanced intermediate-period amplification at basin sites that directly impacts mid-rise building performance. The comprehensive disaggregation results enable systematic development of design ground motion suites capturing controlling earthquake scenarios across the magnitude-distance spectrum, providing quantitative foundations for performance-based seismic design applications. The demonstrated multi-segment rupture potential fundamentally challenges conventional fault segmentation approaches in building code development, necessitating revised source characterization methodologies that acknowledge demonstrated cascading failure mechanisms.

This investigation establishes important precedents for comprehensive seismic hazard assessment in complex tectonic environments, demonstrating the effectiveness of complementary probabilistic and physics-based validation approaches for continental transform systems. The systematic treatment of multi-segment rupture potential provides quantitative frameworks for addressing similar challenges in other major fault systems

worldwide, including the North Anatolian Fault, San Andreas Fault, and Alpine Fault systems where complex segmentation architectures present comparable assessment challenges. The physics-based validation establishes important benchmarks for numerical modeling accuracy while identifying specific application domains where current methodologies excel or require enhancement.

## Conclusion

This comprehensive seismic hazard assessment for the East Anatolian Fault Zone establishes quantitative foundations for evidence-based seismic design and risk mitigation strategies while advancing methodological frameworks for complex continental transform systems. The investigation makes four primary contributions to seismic hazard science and engineering applications.

First, and representing the primary methodological innovation, the probabilistic seismic hazard assessment systematically quantifies multi-segment rupture potential through novel source model configurations (ISM, LMSM, EMSM) that explicitly treat the cascading failure mechanisms demonstrated by the 2023 earthquake sequence. This framework fundamentally challenges conventional independent segment assumptions that have dominated seismic hazard practice, providing the first systematic probabilistic treatment of complex rupture scenarios for EAFZ. The comprehensive assessment reveals pronounced spatial variations with maximum peak ground acceleration values approaching 2.0g for 2475-year return periods, concentrated along a well-defined high-hazard corridor extending throughout the fault system. Site-specific hazard characterization demonstrates severe seismic exposure at major urban centers, with Elazığ and Hatay/Antakya experiencing 475-year design ground motions of 0.567g and 0.557g respectively, substantially exceeding conventional building code provisions for high seismic zones. The novel multi-segment source characterization provides quantitative frameworks for treating fault segments as interconnected components rather than independent seismic sources, directly addressing the demonstrated 370 km cascading rupture that transcended traditional segmentation boundaries during the Kahramanmaraş event.

Second, the physics-based simulation provides comprehensive validation of SPECFEM3D kinematic modeling against the 2023 continental transform earthquake, establishing quantitative benchmarks for numerical modeling accuracy across diverse distance and geological conditions. The validation framework demonstrates exceptional performance characteristics at intermediate distances (20-80 km), where synthetic predictions achieve synthetic-to-observed amplitude ratios within 0.8-1.2 across all components, establishing

reliable application domains for current kinematic implementations. Near-fault environments present systematic amplitude underestimation of 25-35%, reflecting kinematic source limitations in reproducing complex high-frequency radiation patterns and directivity effects characteristic of strike-slip ruptures. This quantified accuracy assessment provides essential confidence bounds for the regional seismo-tectonic framework including the 13-layer velocity structure, fault geometry parameterization, and crustal properties that inform ground motion prediction across the study region.

Third, the comprehensive epistemic uncertainty quantification through systematic logic tree implementation encompassing 162 branches establishes robust methodological frameworks for addressing complex fault system uncertainties in regional hazard assessment applications. The spectral acceleration characterization reveals systematic period-dependent variations critical for engineering design, with short-period accelerations exceeding 2.2g and significant intermediate-period amplification at sedimentary basin sites reaching 0.98g at 0.5-second periods. Disaggregation analysis identifies systematic site-specific controlling earthquake scenarios, with near-source locations dominated by proximal large-magnitude events (Mw6.8 at 5km) while off-fault sites depend on distant high-magnitude scenarios (Mw6.8 at 65km), providing essential guidance for scenario-based design and risk assessment. The three-dimensional magnitude-distance-epsilon analysis demonstrates that design-level ground motions are achieved through median-level earthquake scenarios rather than requiring extreme residual contributions, enabling reliable extrapolation to extreme return period scenarios essential for critical infrastructure applications.

Fourth, the research establishes updated seismic hazard estimates incorporating lessons learned from the 2023 earthquake observations, with direct implications for seismic design criteria, building code development, and emergency preparedness strategies across seismically active regions globally. The comprehensive disaggregation results enable systematic development of design ground motion suites capturing controlling earthquake scenarios across the magnitude-distance spectrum, providing quantitative foundations for performance-based seismic design applications. The demonstrated multi-segment rupture potential fundamentally challenges conventional fault segmentation approaches in building code development, necessitating revised source characterization methodologies that acknowledge demonstrated cascading failure mechanisms in complex continental transform systems.

Priority research directions should focus on implementation of dynamic rupture modeling to enhance near-fault prediction accuracy, addressing systematic limitations identified in kinematic source approaches for complex high-frequency ground motion generation.

Development of time-dependent hazard assessment frameworks incorporating stress transfer effects and temporal clustering patterns observed in recent earthquake sequences represent a critical advancement for capturing evolving seismic risk in complex fault systems. Advanced site characterization methodologies incorporating detailed basin structure modeling and three-dimensional velocity architectures will improve local site response predictions, particularly for sedimentary environments where significant amplification effects influence engineering applications. Real-time seismic monitoring networks deployed alongside physics-based simulation capabilities enable rapid post-earthquake ground-motion assessment for emergency response coordination. The methodological frameworks developed here serve as practical tools for addressing multi-segment rupture problems across diverse fault systems globally, creating platforms for future advances in computational seismology, earthquake physics, and quantitative hazard assessment. Through complementary deployment of comprehensive probabilistic frameworks for multi-segment rupture quantification, supported by physics-based validation of regional modeling capability, this investigation advances understanding of complex fault-system behavior and provides robust quantitative foundations for enhanced seismic preparedness and risk mitigation strategies

## Reference

- Abrahamson, N. A., Silva, W. J., & Kamai, R. (2014). Summary of the ASK14 ground motion relation for active crustal regions. *Earthquake Spectra*, 30(3), 1025–1055.
- AFAD. (2023, February 6). *AFAD (2023). 06 Şubat 2023 Pazarcık-Elbistan Kahramanmaraş (Mw: 7.7 – Mw: 7.6) Depremleri Raporu. Disaster and Emergency Management Presidency, Ankara*.
- Akkar, S., & Cagnan, Z. (2010). A Local Ground-Motion Predictive Model for Turkey, and Its Comparison with Other Regional and Global Ground-Motion Models. *Bulletin of the Seismological Society of America*, 100(6), 2978–2995. <https://doi.org/10.1785/0120090367>
- Akkar, S., Sandikkaya, M. A., & Bommer, J. J. (2014). Empirical ground-motion models for point- and extended-source crustal earthquake scenarios in Europe and the Middle East. *Bulletin of Earthquake Engineering*, 12(1), 359–387.
- Aktuğ, B., Parmaksız, E., Kurt, M., Lenk, O., Kılıçoglu, A., Gürdal, M. A., & Özdemir, S. (2016). Deformation of Central Anatolia: GPS implications. *Journal of Geodynamics*, 67, 78–96.
- Al-Lazki, A. I., Seber, D., Sandvol, E., Turkelli, N., Mohamad, R., & Barazangi, M. (2003). Tomographic Pn velocity and anisotropy structure beneath the Anatolian plateau (eastern Turkey) and the surrounding regions. *Geophysical Research Letters*, 30(24). <https://doi.org/10.1029/2003GL017391>
- Baker, J. W. (2013). *An introduction to probabilistic seismic hazard analysis. White paper version 2.1*.
- Barbot, S., Luo, H., Wang, T., Hamiel, Y., Piatibratova, O., Javed, M. T., Brautenberg, C., & Gurbuz, G. (2023). Slip distribution of the February 6, 2023 Mw 7.8 and Mw 7.6, Kahramanmaraş, Turkey earthquake sequence in the East Anatolian Fault Zone. *Seismica*, 2(3). <https://doi.org/10.26443/seismica.v2i3.502>
- Bayless, J., & Abrahamson, N. A. (2019). Summary of the BA18 Ground-Motion Model for Fourier Amplitude Spectra for Crustal Earthquakes in California. *Bulletin of the Seismological Society of America*, 109(5), 2088–2105. <https://doi.org/10.1785/0120190077>
- Ben-Zion, Y., & Sammis, C. G. (2003). Characterization of Fault Zones. *Pure and Applied Geophysics*, 160(3), 677–715. <https://doi.org/10.1007/PL00012554>

- Biasi, G. P., & Wesnousky, S. G. (2016). Steps and Gaps in Ground Ruptures: Empirical Bounds on Rupture Propagation. *Bulletin of the Seismological Society of America*, 106(3), 1110–1124. <https://doi.org/10.1785/0120150175>
- Biasi, G. P., & Wesnousky, S. G. (2017). Bends and Ends of Surface Ruptures. *Bulletin of the Seismological Society of America*, 107(6), 2543–2560. <https://doi.org/10.1785/0120160292>
- Bommer, J. J., Douglas, J., Scherbaum, F., Cotton, F., Bungum, H., & Fah, D. (2010). On the Selection of Ground-Motion Prediction Equations for Seismic Hazard Analysis. *Seismological Research Letters*, 81(5), 783–793. <https://doi.org/10.1785/gssrl.81.5.783>
- Boore, D. M., & Atkinson, G. M. (2008). Ground-motion prediction equations for the average horizontal component of PGA, PGV, and 5%-damped PSA at spectral periods between 0.01 s and 10.0 s. *Earthquake Spectra*, 24(1), 99–138. <https://doi.org/10.1193/1.2830434>
- Bradley, B. A. (2013). A critical examination of seismic response uncertainty analysis in earthquake engineering. *Earthquake Engineering & Structural Dynamics*, 42(11), 1717–1729. <https://doi.org/10.1002/eqe.2331>
- Campbell, K. W., & Bozorgnia, Y. (2014). NGA-West2 ground motion model for the average horizontal components of PGA, PGV, and 5% damped linear acceleration response spectra. *Earthquake Spectra*, 30(3), 1087–1115.
- Cavalié, O., & Jónsson, S. (2014). Block-like plate movements in eastern Anatolia observed by InSAR. *Geophysical Research Letters*, 41(1), 26–31. <https://doi.org/10.1002/2013GL058170>
- Çetin, H., Güneyli, H., & Mayer, L. (2003). Paleoseismology of the Palu–Lake Hazar segment of the East Anatolian Fault Zone, Turkey. *Tectonophysics*, 374(3–4), 163–197.
- Chiou, B. S. J., & Youngs, R. R. (2014). Update of the Chiou and Youngs NGA model for the average horizontal component of peak ground motion and response spectra. *Earthquake Spectra*, 30(3), 1117–1153.
- Cornell, C. A. (1968). ENGINEERING SEISMIC RISK ANALYSIS. In *Bulletin of the Seismological Society of America* (Vol. 58, Issue 5).
- Duman, T. Y., & Emre, Öm. (2013). The east anatolian fault: Geometry, segmentation and jog characteristics. *Geological Society Special Publication*, 372(1), 495–529. <https://doi.org/10.1144/SP372.14>

- Emre, Ö., Duman, T. Y., Özalp, S., Saroğlu, F., Olgun, Ş., Elmacı, H., & Çan, T. (2018). Active fault database of Turkey. *Bulletin of Earthquake Engineering*, 16(8), 3229–3275. <https://doi.org/10.1007/s10518-016-0041-2>
- Faccenna, C., Bellier, O., Martinod, J., Piromallo, C., & Regard, V. (2006). Slab detachment beneath eastern Anatolia: A possible cause for the formation of the North Anatolian fault. *Earth and Planetary Science Letters*, 242(1–2), 85–97. <https://doi.org/10.1016/j.epsl.2005.11.046>
- Field, E. H., Arrowsmith, R. J., Biasi, G. P., Bird, P., Dawson, T. E., Felzer, K. R., Jackson, D. D., Johnson, K. M., Jordan, T. H., Madden, C., Michael, A. J., Milner, K. R., Page, M. T., Parsons, T., Powers, P. M., Shaw, B. E., Thatcher, W. R., Weldon, R. J., & Zeng, Y. (2014). Uniform California Earthquake Rupture Forecast, Version 3 (UCERF3)--The Time-Independent Model. *Bulletin of the Seismological Society of America*, 104(3), 1122–1180. <https://doi.org/10.1785/0120130164>
- Global Earthquake Model Foundation. (2025a). *Global Seismic Hazard Map*. <Https://Maps.Openquake.Org/Map/Global-Seismic-Hazard-Map/#8/37.571/37.227>.
- Global Earthquake Model Foundation. (2025b). *OpenQuake Engine 3.23.1*. Global Earthquake Model (GEM). <https://github.com/gem/oq-engine/releases/tag/v3.23.1>
- Graves, R., Jordan, T. H., Callaghan, S., Deelman, E., Field, E., Juve, G., Kesselman, C., Maechling, P., Mehta, G., Milner, K., Okaya, D., Small, P., & Vahi, K. (2011). CyberShake: A Physics-Based Seismic Hazard Model for Southern California. *Pure and Applied Geophysics*, 168(3–4), 367–381. <https://doi.org/10.1007/s00024-010-0161-6>
- Graves, R., & Pitarka, A. (2015). Refinements to the Graves and Pitarka (2010) Broadband Ground-Motion Simulation Method. *Seismological Research Letters*, 86(1), 75–80. <https://doi.org/10.1785/0220140101>
- Graves, R., & Pitarka, A. (2016). Kinematic Ground-Motion Simulations on Rough Faults Including Effects of 3D Stochastic Velocity Perturbations. *Bulletin of the Seismological Society of America*, 106(5), 2136–2153. <https://doi.org/10.1785/0120160088>
- Herece, E. (2008). *Atlas of East anatolian fault*. General Directorate of Mineral Research and Exploration (MTA), Special Publication Series.
- Jia, Z., Jin, Z., Marchandon, M., Ulrich, T., Gabriel, A.-A., Fan, W., Shearer, P., Zou, X., Rekoske, J., Bulut, F., Garagon, A., & Fialko, Y. (2023). The complex dynamics of the 2023 Kahramanmaraş, Turkey,  $M_w$  7.8-7.7 earthquake doublet. *Science*, 381(6661), 985–990. <https://doi.org/10.1126/science.adl0685>

- Kahraman, M., Cornwell, D. G., Thompson, D. A., Rost, S., Houseman, G. A., Türkelli, N., Teoman, U., Altuncu Poyraz, S., Utkucu, M., & Gülen, L. (2015). Crustal-scale shear zones and heterogeneous structure beneath the North Anatolian Fault Zone, Turkey, revealed by a high-density seismometer array. *Earth and Planetary Science Letters*, 430, 129–139. <https://doi.org/10.1016/j.epsl.2015.08.014>
- Kawase, H. (1996). *The Cause of the Damage Belt in Kobe: "The Basin-Edge Effect, " Constructive Interference of the Direct S-Wave with the Basin-Induced Diffracted/Rayleigh Waves.*
- Komatitsch, D., & Tromp, J. (2002). Spectral-element simulations of global seismic wave propagation - I. Validation. *Geophysical Journal International*, 149(2), 390–412. <https://doi.org/10.1046/j.1365-246X.2002.01653.x>
- Kotha, S. R., Weatherill, G., Bindi, D., & Cotton, F. (2020). A regionally-adaptable ground-motion model for shallow crustal earthquakes in Europe. *Bulletin of Earthquake Engineering*, 18(9), 4091–4125. <https://doi.org/10.1007/s10518-020-00869-1>
- Mahmoud, Y., Masson, F., Meghraoui, M., Cakir, Z., Alchalbi, A., Yavasoglu, H., Yönlü, O., Daoud, M., Ergintav, S., & Inan, S. (2013). Kinematic study at the junction of the East Anatolian fault and the Dead Sea fault from GPS measurements. *Journal of Geodynamics*, 67, 30–39. <https://doi.org/10.1016/j.jog.2012.05.006>
- Mai, P. M., & Beroza, G. C. (2002). A spatial random field model to characterize complexity in earthquake slip. *Journal of Geophysical Research: Solid Earth*, 107(B11). <https://doi.org/10.1029/2001jb000588>
- Marzocchi, W., Taroni, M., & Selva, J. (2015). Accounting for Epistemic Uncertainty in PSHA: Logic Tree and Ensemble Modeling. *Bulletin of the Seismological Society of America*, 105(4), 2151–2159. <https://doi.org/10.1785/0120140131>
- McClusky, S., Balassanian, S., Barka, A., Demir, C., Ergintav, S., Georgiev, I., Gurkan, O., Hamburger, M., Hurst, K., Kahle, H., Kastens, K., Kekelidze, G., King, R., Kotzev, V., Lenk, O., Mahmoud, S., Mishin, A., Nadariya, M., Ouzounis, A., ... Veis, G. (2000). Global Positioning System constraints on plate kinematics and dynamics in the eastern Mediterranean and Caucasus. *Journal of Geophysical Research: Solid Earth*, 105(B3), 5695–5719. <https://doi.org/10.1029/1999jb900351>
- McGuire, J. J. (2004). Estimating Finite Source Properties of Small Earthquake Ruptures. *Bulletin of the Seismological Society of America*, 94(2), 377–393. <https://doi.org/10.1785/0120030091>

- Melgar, D., Taymaz, T., Ganas, A., Crowell, B., Öcalan, T., Kahraman, M., Tsironi, V., Yolsal-Çevikbil, S., Valkaniotis, S., Irmak, T. S., Eken, T., Erman, C., Özkan, B., Dogan, A. H., & Altuntaş, C. (2023). Sub- and super-shear ruptures during the 2023 Mw 7.8 and Mw 7.6 earthquake doublet in SE Türkiye. *Seismica*, 2(3). <https://doi.org/10.26443/seismica.v2i3.387>
- Mutlu, A. K., & Karabulut, H. (2011). Anisotropic Pn tomography of Turkey and adjacent regions. *Geophysical Journal International*, 187(3), 1743–1758. <https://doi.org/10.1111/j.1365-246X.2011.05235.x>
- Olsen, K. B. (2000). Site Amplification in the Los Angeles Basin from Three-Dimensional Modeling of Ground Motion. *Bulletin of the Seismological Society of America*, 90(6B), S77–S94. <https://doi.org/10.1785/0120000506>
- Olsen, K. B., Day, S. M., Minster, J. B., Cui, Y., Chourasia, A., Faerman, M., Moore, R., Maechling, P., & Jordan, T. (2006). Strong shaking in Los Angeles expected from southern San Andreas earthquake. *Geophysical Research Letters*, 33(7). <https://doi.org/10.1029/2005GL025472>
- Özacar, A. A., Zandt, G., Gilbert, H., & Beck, S. L. (2010). Seismic images of crustal variations beneath the East Anatolian Plateau (Turkey) from teleseismic receiver functions. *Geological Society, London, Special Publications*, 340(1), 485–496. <https://doi.org/10.1144/SP340.21>
- Pagani, M., Monelli, D., Weatherill, G., Danciu, L., Crowley, H., Silva, V., Henshaw, P., Butler, L., Nastasi, M., Panzeri, L., Simionato, M., & Vigano, D. (2014). OpenQuake Engine: An Open Hazard (and Risk) Software for the Global Earthquake Model. *Seismological Research Letters*, 85(3), 692–702. <https://doi.org/10.1785/0220130087>
- Peter, D., Komatitsch, D., Luo, Y., Martin, R., Le Goff, N., Casarotti, E., Le Loher, P., Magnoni, F., Liu, Q., Blitz, C., Nissen-Meyer, T., Basini, P., & Tromp, J. (2011). Forward and adjoint simulations of seismic wave propagation on fully unstructured hexahedral meshes. *Geophysical Journal International*, 186(2), 721–739. <https://doi.org/10.1111/j.1365-246X.2011.05044.x>
- Pousse-Beltran, L., Nissen, E., Bergman, E. A., Cambaz, M. D., Gaudreau, É., Karasözen, E., & Tan, F. (2020). The 2020  $M_w$  6.8 Elazığ (Turkey) Earthquake Reveals Rupture Behavior of the East Anatolian Fault. *Geophysical Research Letters*, 47(13). <https://doi.org/10.1029/2020GL088136>
- Reilinger, R., McClusky, S., Vernant, P., Lawrence, S., Ergintav, S., Cakmak, R., Ozener, H., Kadirov, F., Guliev, I., Stepanyan, R., Nadariya, M., Hahubia, G., Mahmoud, S., Sakr,

K., ArRajehi, A., Paradissis, D., Al-Aydrus, A., Prilepin, M., Guseva, T., ... Karam, G. (2006). GPS constraints on continental deformation in the Africa-Arabia-Eurasia continental collision zone and implications for the dynamics of plate interactions. *Journal of Geophysical Research: Solid Earth*, 111(5). <https://doi.org/10.1029/2005JB004051>

Rodgers, A. J., Anders Petersson, N., Pitarka, A., McCallen, D. B., Sjogreen, B., & Abrahamson, N. (2019). Broadband (0–5 Hz) Fully Deterministic 3D Ground-Motion Simulations of a Magnitude 7.0 Hayward Fault Earthquake: Comparison with Empirical Ground-Motion Models and 3D Path and Site Effects from Source Normalized Intensities. *Seismological Research Letters*, 90(3), 1268–1284. <https://doi.org/10.1785/0220180261>

Sandvol, E., Turkelli, N., Zor, E., Gok, R., Bekler, T., Gurbuz, C., Seber, D., & Barazangi, M. (2003). Shear wave splitting in a young continent-continent collision: An example from Eastern Turkey. *Geophysical Research Letters*, 30(24). <https://doi.org/10.1029/2003GL017390>

Schwartz, D. P., & Coppersmith, K. J. (1984). Fault behavior and characteristic earthquakes: Examples from the Wasatch and San Andreas Fault Zones. *Journal of Geophysical Research: Solid Earth*, 89(B7), 5681–5698. <https://doi.org/10.1029/JB089iB07p05681>

Stein, R. S. (1999). The role of stress transfer in earthquake occurrence. In *NATURE* (Vol. 402). [www.nature.com](http://www.nature.com)

Stewart, J. P., Douglas, J., Javanbarg, M., Bozorgnia, Y., Abrahamson, N. A., Boore, D. M., Campbell, K. W., Delavaud, E., Erdik, M., & Stafford, P. J. (2015). Selection of Ground Motion Prediction Equations for the Global Earthquake Model. *Earthquake Spectra*, 31(1), 19–45. <https://doi.org/10.1193/013013EQS017M>

Stirling, M., McVerry, G., Gerstenberger, M., Litchfield, N., Van Dissen, R., Berryman, K., Barnes, P., Wallace, L., Villamor, P., Langridge, R., Lamarche, G., Nodder, S., Reyners, M., Bradley, B., Rhoades, D., Smith, W., Nicol, A., Pettinga, J., Clark, K., & Jacobs, K. (2012). National Seismic Hazard Model for New Zealand: 2010 Update. *Bulletin of the Seismological Society of America*, 102(4), 1514–1542. <https://doi.org/10.1785/0120110170>

Taborda, R., Azizzadeh-Roodpis, S., Khoshnevis, N., & Cheng, K. (2016). Evaluation of the southern California seismic velocity models through simulation of recorded events. *Geophysical Journal International*, 205(3), 1342–1364. <https://doi.org/10.1093/gji/ggw085>

- Taborda, R., & Bielak, J. (2014). Ground-Motion Simulation and Validation of the 2008 Chino Hills, California, Earthquake Using Different Velocity Models. *Bulletin of the Seismological Society of America*, 104(4), 1876–1898. <https://doi.org/10.1785/0120130266>
- Tezel, T., Shibutani, T., & Kaypak, B. (2013). Crustal thickness of Turkey determined by receiver function. *Journal of Asian Earth Sciences*, 75, 36–45. <https://doi.org/10.1016/j.jseaes.2013.06.016>
- UNDP. (2023). *Recovery and Reconstruction after the 2023 Earthquakes in Türkiye UNDP offer and proposed projects*.
- United States Geological Survey. (2023). *USGS Event Page for Mw 7.8 Kahramanmaraş Earthquake*. USGS. <https://earthquake.usgs.gov/earthquakes/eventpage/us6000jllz/executive>
- Wells, D. L., & Coppersmith, K. J. (1994). New empirical relationships among magnitude, rupture length, rupture width, rupture area, and surface displacement. *Bulletin - Seismological Society of America*, 84(4), 974–1002. <https://doi.org/10.1785/bssa0840040974>
- Wesnousky, S. G. (2006). Predicting the endpoints of earthquake ruptures. *Nature*, 444(7117), 358–360. <https://doi.org/10.1038/nature05275>
- Westaway, R. (2003). *Kinematics of the Middle East and Eastern Mediterranean Kinematics of the Middle East and Eastern Mediterranean Updated Updated ROB WESTAWAY*. <https://journals.tubitak.gov.tr/earth/>
- Westaway, R. (2004). Kinematic consistency between the Dead Sea Fault Zone and the Neogene and Quaternary left-lateral faulting in SE Turkey. *Tectonophysics*, 391(1–4), 203–237. <https://doi.org/10.1016/j.tecto.2004.07.014>
- Withers, K. B., Olsen, K. B., Day, S. M., & Shi, Z. (2019). Ground Motion and Intraevent Variability from 3D Deterministic Broadband (0–7.5 Hz) Simulations along a Nonplanar Strike-Slip Fault. *Bulletin of the Seismological Society of America*, 109(1), 229–250. <https://doi.org/10.1785/0120180006>